Electrocatalysis (2020) 11:465–484
https://doi.org/10.1007/s12678-020-00608-9

REVIEW ARTICLE

Recent Advances in Nanocasting Cobalt-Based Mesoporous Materials for Energy Storage and Conversion

Ali Saad[1] · Zhixing Cheng[1] · Hangjia Shen[1] · Tiju Thomas[2] · Minghui Yang[1]

Published online: 5 June 2020

Abstract

The generation of novel mesoporous materials with well-defined structure and accessible pore networks is helpful in both fundamental and energy-related research. Nanocasting mesoporous earth-abundant materials and their composite materials offer opportunities to make electrochemically active materials that allow scalable production and cost-effectiveness. Recently, due to their intrinsic open pore structure as well as high surface areas, various mesoporous cobalt-based ordered materials have been applied to electrocatalysis, rechargeable batteries, and supercapacitors. In this review, we have critically evaluated the advancements made specifically in three- and two-dimensionally (3D/2D) electrode Co-based materials (oxides, nitrides, phosphides, and sulfides). We outline foreseeable challenges and issues for the utilization of mesostructured cobalt-based electrode materials. This review also provides guidelines for further work to those who work on energy-related applications of mesoporous cobalt-based materials.

Keywords Mesoporous cobalt-based materials · Nanocasting · Electrocatalysis · Rechargeable batteries · Supercapacitors

Introduction

Significant effort has been put in to develop highly active, selective, and low-cost catalytically active electrode materials for energy systems [1]. Low-cost earth-abundant materials are rapidly rising as promising alternatives for energy production and conversion. In particular, mesoporous cobalt-based materials have attracted more attention due to their low-cost, natural abundance, and superior catalytic performance [2–4]. These materials play a significant role in determining the cell efficiency and stability. This is due to their excellent chemical resistance and good conductivity [5, 6]. The interaction of electrolyte within the porous structure is governed by a combination of factors including morphology, porosity, chemical nature, and roughness of the surface. Consequently, mesoporous metal materials have garnered the attention of researchers in electrochemistry due to their large surface area, their interconnected pore structure, and their abundant density of active sites. They hence offer a means to improve the electrochemical performances of batteries [7].

Important advances have been made during the past decades to synthesize several mesoporous cobalt-based oxides and their derivatives. Mesoporous cobalt-based compounds have been prepared by different synthesis routes. For instance, soft-templating routes have been used to synthesize cobalt-based porous transition metal compounds [8]. However, these materials are often poorly crystallized and have poor crystalline order due to significant charge mismatch between the hydrophobic surfactant and solubilized inorganic precursor species. This in fact limits their applications [9]. To maximize control of pore size and surface structure, hard templating, also known as nanocasting, is used. This approach can create mesostructured materials which are harder to obtain by conventional processes using mainly inorganic nanostructures as the endo- or exotemplate [10, 11]. Primarily driven by confinement of mixed metal precursors in the nanopores of a given template, nanocasting has been widely applied to prepare several mesoporous multi-metal materials such as mixed

✉ Tiju Thomas
tt332@cornell.edu; tijuthomas@iitm.ac.in

✉ Minghui Yang
myang@nimte.ac.cn

[1] Solid State Functional Materials Research Laboratory, Ningbo Institute of Materials Technology and Engineering (NIMTE), Chinese Academy of Sciences (CAS), Ningbo 315201, China

[2] Department of Metallurgical and Materials Engineering, Indian Institute of Technology Madras, Adyar, Chennai, Tamil Nadu 600036, India

oxides [12–14], perovskites [15, 16], metal carbides [17], phosphides [18–20], nitrides [21], and intermetallic nanostructures [22]. Based on the above considerations, nanocasting cobalt nanostructures (oxides, nitrides, phosphides, and sulfides) in different nanoarchitectural forms open up fresh avenues for obtaining active electrode materials for future energy application.

The current review will focus on the recent design and synthesis of a wide range of materials including oxides, nitrides, phosphides, and sulfides. The structural features of resulting materials and a summary of their electrochemical performances will be discussed. Moreover, we point out the current prospects and challenges. This work will allow a comprehensive evaluation of the effect of mesoporous structures and nanoarchitectures for improving performance in applications involving energy storage, energy conversion, and hydrogen production.

Nanocasting Synthesis Route

The nanocasting or hard template route initiated by the group of Ryo is an attractive route for the synthesis of mesoporous non-silica mesostructured materials [23]. Commonly, this method is employed to generate various materials that are difficult to achieve through conventional processes of self-assembly. The method involves uses of templates structure-directing agents for the construction of metal materials [24–26], benchmarking electrocatalysts Ru- and Ir-based oxides [27, 28], non-precious metal materials [29, 30], and noble metal-doped non-precious metal materials [31]. This process involves multiple steps: (i) the preparation of ordered mesoporous silica with extremely high values of specific surface area as the hard template, (ii) impregnation of the metal precursor into the pores, and (iii) finally removal of the hard template by a chemical or thermal treatment [32]. After removal of the original template, what is left behind is an inverse replica with highly crystalline walls and good thermal stability. The template is removed by a chemical etching method, which involves a strong acid/base (NaOH or HF) [33, 34]. Consequently, repeated hard-templating procedures (say done twice) help in achieving a very high degree of pore filling and yield direct copies with similar nanostructure as the mother template [35]. Especially, uniform mesoporous silica such as SBA-15 and KIT-6 are commonly used as a hard template due to their diverse pore architectures and extremely uniform pore size. The silica matrix serves as a rigid skeleton, allowing for the metal oxide to crystallize without growing to larger size [36]. Figure 1 shows a schematic representation for synthesizing mesoporous materials in which ordered cylindrical SBA-15 is used as an example of hard templates.

The facile approach outlined above is readily applicable to most of the earth-abundant materials, having a large specific surface area. These nanostructured materials are found to be useful for a multitude of applications such as catalysts, sensors, and batteries [37–39]. Moreover, it is possible to achieve solid/solid transformations in mesoporous solids through a nanocasting process, while maintaining the mesostructure. An example of this would be the conversion of mesoporous Co_3O_4 to CoO [40], transformation of mesoporous Co_3O_4 to $LiCoO_2$ [41], and synthesis of heterostructured mesoporous material $Co_3O_4/CoFe_2O_4$ via a simple solid−solid reaction of an iron precursor with ordered mesoporous Co_3O_4 [42]. More interestingly, it is possible to synthesis mesoporous metal material derivates via sulfurization, phosphorization, and nitridation. Shi and coworkers introduced an ammonia nitridation approach through a gas−solid reaction for the first reports on the synthesis of ordered mesoporous nitrides CoN and CrN [43].

Nanocasting Mesoporous Cobalt-Based Oxides

Cobalt-based metal oxides have been widely used in energy conversion and storage for water oxidation, supercapacitors, and batteries. Nanostructuring of the surface and incorporation into supporting silica scaffolds has led to stable, high rate catalysts [44]. Here we highlight the applications of cobalt-based ordered mesoporous metal oxides in energy conversion and storage.

Oxygen Evolution Electrocatalysis for Water Splitting

Electrochemical water oxidation is a reaction generating molecular oxygen and production of hydrogen through several proton-/electron-coupled processes. The overall water oxidation involves active electrocatalysis towards the anodic oxygen evolution reaction (OER) [45]. Nanocast mesoporous cobalt oxides owing to their low-cost and high intrinsic catalytic activity have proven to be useful for the production of oxygen by electrochemical oxidation of water [46].

Many efforts are dedicated to the oxygen evolution reaction associated with nanocast Co-based compounds. In particular, Co_3O_4 has a spinel structure, containing Co^{3+} in octahedral coordination sites and Co^{2+} on tetrahedral coordination sites [47] is regarded as promising for water oxidation electrocatalysis. In order to increase the conductivity of the electrocatalysts, both the composition and structure are varied. This is true across compositions including cobalt oxides [48, 49], cobalt-based spinel-type oxides [50, 51], cobalt-based perovskite-type oxides [15, 52], cobalt-based mixed oxides [53], and transition metal-doped cobalt oxides [54] (Table 1).

To illustrate the approaches reported thus far to enhance the electrocatalytic performance of Co-based compounds, we will undertake detailed discussions on reports available on

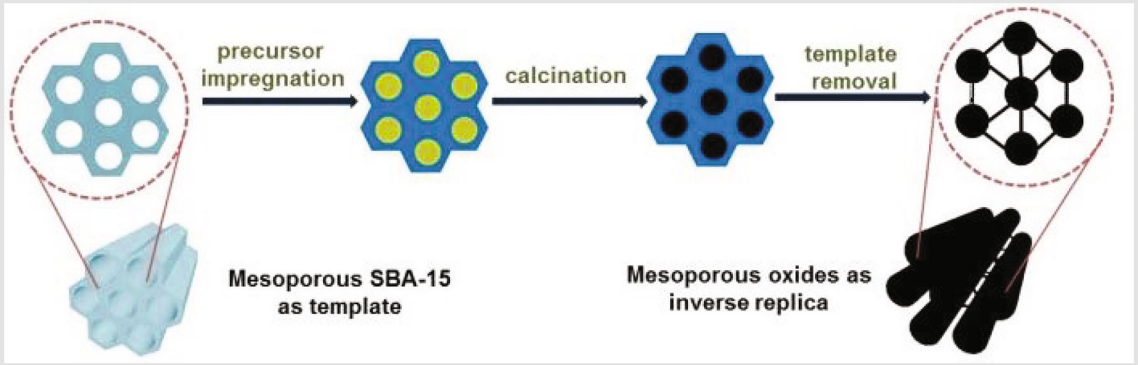

Fig. 1 Schematic representation of the hard-templating process for synthesizing mesoporous metal materials

nanoarchitecture optimization, doping, and utilization of binary cobaltites. Thereafter, we will discuss the utility of these in OER and battery applications.

Nanoarchitecture Optimization

A significant decrease in overpotential occurs as a consequence of the optimization of the surface nanostructure. This approach not only increases the number of active sites on the materials but also changes the intrinsic properties such as binding energy and electroconductivity to the OER intermediate [64]. A good example of this comes from the work of Deng and colleagues [49], who have reported a systematic study on the synthesis of ordered mesoporous Co_3O_4 nanocasting obtained from both of cubically KIT-6 and hexagonally SBA-15 (Fig. 2).

Table 1 Electrochemical performance of nanocasting cobalt-based mesoporous metal materials for oxygen evolution reaction

Nanocasting cobalt-based mesoporous oxides	S_{BET}[a] ($m^2\ g^{-1}$)	Electrolyte	Loading amounts (mg cm^{-2})	Tafel slope (mV dec^{-1})	η[b] (mV) at 10 mA cm^{-2}	Refs.
Meso-Co_3O_4-35	135	0.1 M KOH	0.1	80	411	[55]
Meso-Co_3O_4-100	114	0.1 M KOH	0.1	66	426	[55]
Fe-doped meso-Co_3O_4	102	0.1 M KOH	0.12	-	486	[56]
Meso-$Cu_xCo_yO_4$	126	1 M KOH	0.12	-	391	[50]
Au-meso-Co_3O_4	109	0.1 M NaOH	~ 0.015	46	440	[57]
Meso-Co_3O_4-100	113	0.1 M KOH	0.13	-	636	[48]
Meso-Co_3O_4-35	156	0.1 M KOH	0.13	-	525	[48]
mCo_3O_4	54	1 M KOH	0.075	71.6	420	[54]
Fe/mCo_3O_4	135	1 M KOH	0.075	60.0	380	[54]
Ni/mCo_3O_4	144	1 M KOH	0.075	88	410	[54]
FeNi/mCo_3O_4	136	1 M KOH	0.075	87.2	410	[54]
Ir–Co_3O_4	57.8	1 M KOH	0.1	80.5	293	[58]
Pd–Co_3O_4 (wt 1:1)	81	0.1 M KOH	0.1	60.7	360	[59]
$Co_{2.775}Fe_{0.225}O_4$	22.27	1 M KOH	0.25	58	317	[60]
$Co_3O_{4-\delta}$	92	0.1 M KOH	0.074	-	440	[61]
$MnCo_2O_{4-\delta}$	135	0.1 M KOH	0.074	-	530	[61]
$NiCo_2O_{4-\delta}$	84	0.1 M KOH	0.074	-	390	[61]
MCM-41-$CoFe_2O_4$	165.5	1 M KOH	0.142	85.2	383	[51]
KIT-6-100-$CoFe_2O$	151.6	1 M KOH	0.142	58.4	360	[51]
SBA-15-120-$CoFe_2O_4$	163.3	1 M KOH	0.142	57.1	342	[51]
Co/Ni (4/1)	94	1 M KOH	0.12	36	336	[62]
$Ni_{0.60}Co_{2.40}O_4$	107	1 M KOH	0.2	48	330	[14]
$Ba_{0.5}Sr_{0.5}Co_{0.8}Fe_{0.2}O_{3-\delta}$	32.1	0.1 M KOH	-	62	400	[52]
$NiCo_2O_4$	155	1 M KOH	0.14	43	~350	[63]

[a] Brunauer–Emmett–Teller (BET) surface

[b] Overpotential

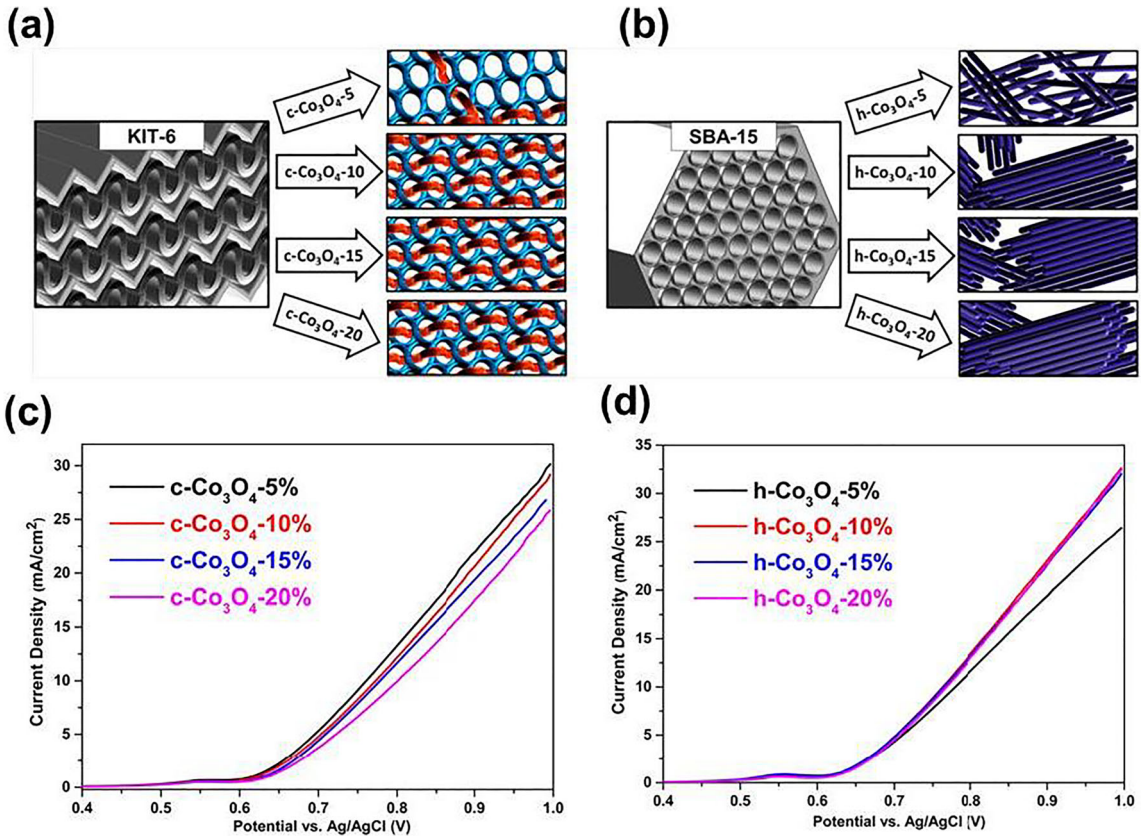

Fig. 2 **a** Schematic illustration of replication of ordered mesoporous cobalt oxides with loading amounts of metal precursors (5%, 10%, 15% replicated from 3D cubic KIT-6 2D and **b** replicated from hexagonal SBA-15 and 20%). **c** The oxygen evolution reaction polarization curves for Co_3O_4 replicated from KIT-6 and **d** from SBA-15. Reproduced with permission from ref. [49]. Copyright 2014, American Chemical Society

By varying the loading amounts of metals precursors filled on the mesoporous silica (5%, 10%, 15%, and 20%), they investigated the outcome on morphologies and the electrocatalytic oxygen evolution activities. It is reported that the cubically ordered Co_3O_4 replicas, the one with a 5% loading amount, exhibits the lowest symmetry and the open pore system obtained thus has the best catalytic water oxidation performance compared with others loading amounts (Fig. 2c). On the other hand, for hexagonally ordered Co_3O_4 replicated from SBA-15, the highest activity observed is with nanowires that have a higher degree of the ordering and interconnectivity (low loading amount 20%) (Fig. 2d). Besides, results showed that hexagonally ordered Co_3O_4 possesses a superior oxygen evolution.

Doping Metal Elements

Further improvements in mass and specific activities have been achieved through the development of multimetallic cobalt-based metal materials by incorporation of a second metal component.

Currently, for example, Grewe and colleagues [56] study the influence of Fe doping on structure and water oxidation activity of nanocast Co_3O_4. As a result, Fe-incorporated Co_3O_4 shows prominent electrochemical activity comparable with noble metal-based materials. In this context, Xiao et al [54]. investigated the electrochemical oxygen evolution affected by the incorporation of Ni and Fe on mesoporous Co_3O_4. As a result, Fe–mCo_3O_4 composite required an onset potential around 1.52 V versus a reversible hydrogen electrode (RHE) for oxygen evolution reaction. It is considered that the synergistic effect between Co_3O_4 and Fe plays an important role in the performance. Recently, Gao et al. [60] via density functional theory (DFT) calculations demonstrated that the preferential geometrical occupancy of Fe^{3+} cations is in octahedral sites due to the lower formation energy (Fig. 3a). Consequently, mesoporous $Co_{2.775}Fe_{0.225}O_4$ with its maximum Fe^{3+} octahedral sites exhibits the best OER activity (η = 317 mV at a current density of 10 mA cm^{-2}) compared with others Co–Fe composition.

For enhancing kinetics and reducing the overpotential, composition tuning by the addition of noble metals to nanocasting Co_3O_4 is done. Examples include mesoporous Au–mCo_3O_4 composites [57], and Pt, Pd, and Au embedded within mesoporous cobalt oxide [65] and mesoporous Ir–Co_3O_4 [60] (Fig. 3 d and e). For example, to achieve the current density of 10 mA cm^{-2}, the optimized mesoporous Ir–$Co_3O_{4\text{-}1}$ exhibited highly efficient OER catalytic

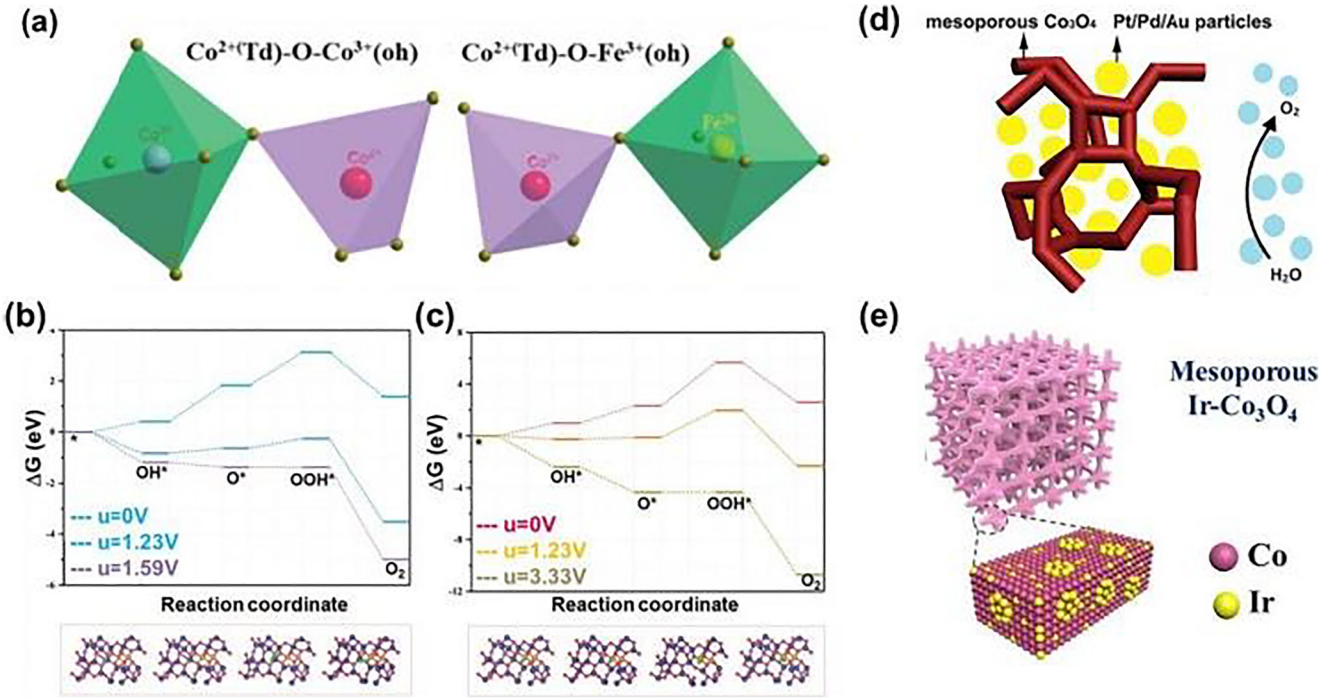

Fig. 3 **a** Schematic representation of the Co^{2+} (Td)–O–Fe^{3+} (Oh) and Co^{2+} (Td)–O–Co^{3+} (Oh) in the spinel structures. **b** The computed Gibbs free energy changes for Co^{2+} (Td)–O–Fe^{3+} (Oh) for the OER where in Co^{3+} (Oh) is treated as the catalytically active centers and **c** Fe^{3+} (Oh) with (H: blue; Co: dark blue; O: red; O: green; Fe: gold). Reproduced with permission from ref. [60]. Copyright 2019, Royal Society of Chemistry. **d** Schematic illustration of Pt, Pd, and Au embedded within mesoporous cobalt oxide. Reproduced with permission from ref. [65]. Copyright 2018, Elsevier. **e** Schematic illustration of 3D cubic Ir-Co_3O_{4-1}. Reproduced with permission from ref. [58]. Copyright 2019, Wiley-VCH

performance with an overpotential of only 293 mV; this results in better OER performance than most of transition metal oxides catalysts reported thus far [58].

Binary Cobaltites

Commonly, binary spinel-type oxides $CoMO_4$ (where M is Ni, Mn, Fe, Cr, etc.) have been widely applied as OER electrocatalysts. Abidat and coworkers reported the synthesis of nanocasting hexagonally $Co_3O_{4-\delta}$, $MnCo_2O_{4-\delta}$, $NiCo_2O_{4-\delta}$, and their OER electroactivity. Herein, benefiting from their synergistic interactions and abundant active catalytic sites, the as-prepared $NiCo_2O_{4-\delta}$ exhibited much better performance towards the OER than $MnCo_2O_{4-\delta}$ and $Co_3O_{4-\delta}$ single metal oxide [61]. Later, they showed the effects of nickel incorporation on a series of mesoporous bicontinuous $Ni_xCo_{3-x}O_4$ materials with a high specific surface area (about 100 $m^2 g^{-1}$) replicated from KIT-6 (Fig. 4) [14]. The most active catalyst is a mesoporous $Ni_{0.60}Co_{2.40}O_4$ sample, which also exhibits the most hydroxylated surface. It required only overpotential of 330 mV to deliver a current density of 10 mA cm^{-2}. Moreover, it was found that these compositions are hydroxylated under oxygen evolution reaction and the amount of surface cobalt hydroxide increases along with a Ni surface enrichment with the Ni content in the catalyst.

Likewise, Deng and coworkers [62] reported the synthesis of a series of mesoporous nickel cobalt oxides through control of the introduced nickel amount (Co/Ni = 8, 4, 2, 1). The catalyst with the optimal composition (Co/Ni:4/1) possesses the lowest overpotential (336 mV) at a current density of 10 mA cm^{-2} with a rather small Tafel slope of 36 mV dec^{-1} compared with other mesoporous Co–Ni compositions. Moreover, they demonstrate the enhancement of water oxidation activity along with the electrochemical measurements in the Fe-free KOH electrolyte. The enhancement of catalytic activity is attributed to the generation of surface $Ni(OH)_2$ species that incorporate Fe impurities from the electrolyte. Furthermore, Broicher et al [63]. have proved via the electrochemical surface area and specific current density comparisons with non-structured nickel cobalt oxides that structuring of mesoporous $NiCo_2O_4$ via KIT-6 improves the intrinsic catalyst performance; this is accompanied by superior charge transfer capacity.

Grewe and coworkers fabricated a series of mesoporous composites based on cobalt by combining Ni, Mo, Cu, Fe, W, and Mn and ordered mesoporous Co_3O_4 through solid −solid reaction transformation/nanocasting approach [50]. This range of composites showed a difference in OER electrocatalytic activity, giving different current densities. A significant improvement in OER performance has been achieved

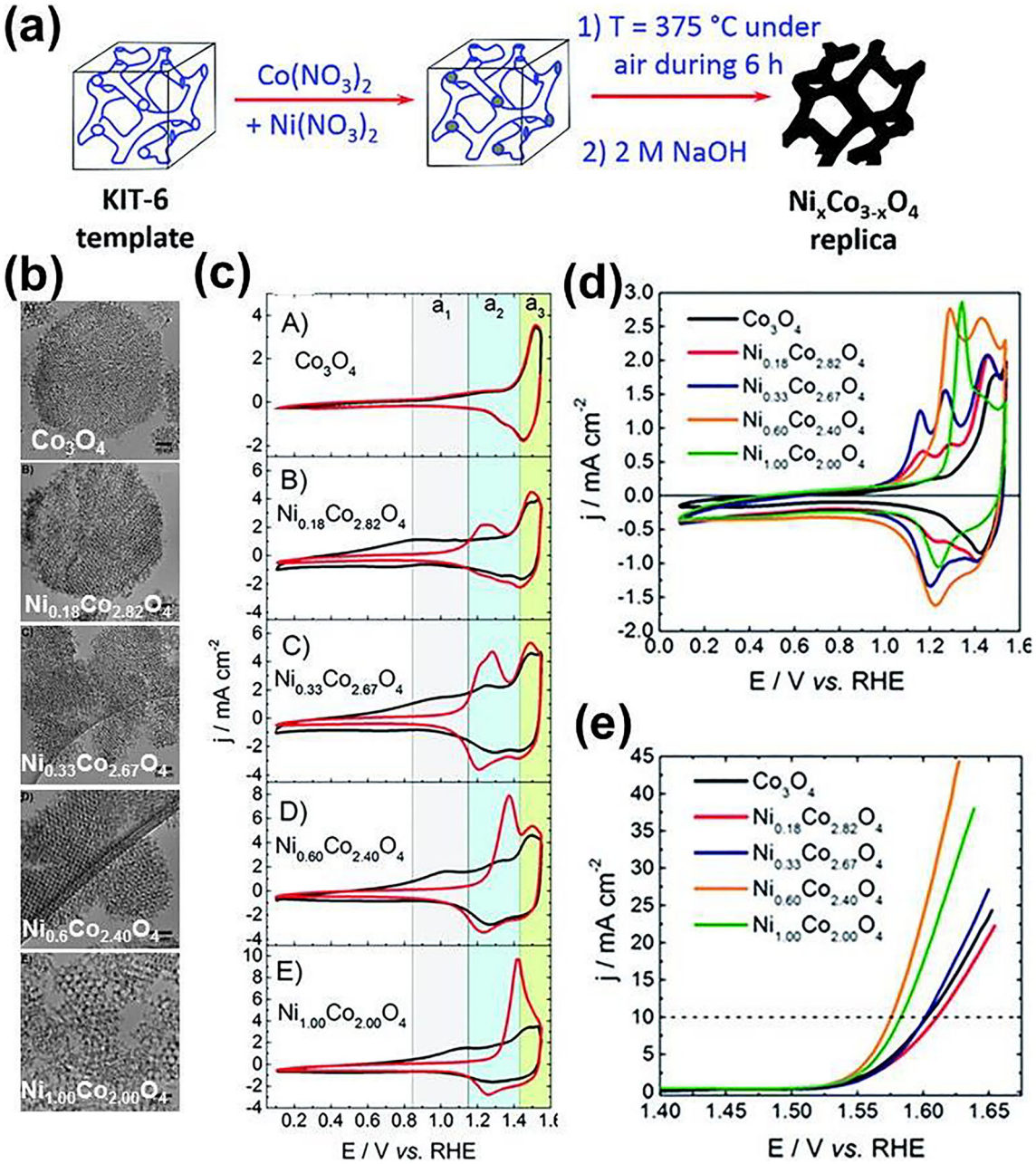

Fig. 4 **a** Schematic diagram of the synthesis of three-dimensional nickel cobaltites, **b** low-magnification TEM images of as-prepared nickel cobaltites, **c** cyclic voltammograms before (black) and after (red) 50 electrochemical cycles recorded in a N_2-saturated KOH 1 mol L^{-1} at a scan rate of 50 mV s^{-1}, **d** low scan rate cyclic voltammograms, **e** OER polarization curves for mesoporous Co_3O_4, $Ni_{0.18}Co_{2.82}O_4$, $Ni_{0.33}Co_{2.67}O_4$, $Ni_{0.60}Co_{2.40}O_4$, and $Ni_{1.00}Co_{2.00}O_4$. Reproduced with permission from ref. [14]. Copyright 2017, Royal Society of Chemistry

for optimized ordered mesoporous $Cu_xCo_yO_4$ (y/x = 8). This offers the lowest onset potential and has relatively higher current densities compared with other mesoporous cobalt-based composites [50]. It is considered that the enhancement of electrocatalytic water oxidation is due to the strong synergistic interactions between Co and Cu. Recently, mesoporous spinel $CoFeO_4$ with 2D and 3D mesoporous structure was reported, as prepared by using a variety of different templates, i.e., SBA-15, KIT-6, and MCM-41 [51]. Compared with other mesoporous spinel Co–Fe nanoarchitectures reported, the resultant hexagonal $CoFe_2O_4$ obtained from SBA-15 exhibits the best OER catalytic activities. In fact, this sample has the smallest overpotential of 342 mV at a current density of 10 mA cm^{-2}. It also has the lowest Tafel slope of 57.1 mV dec^{-1} (Fig. 5) which are also higher than that of the 410 mV and 611 mV dec^{-1} for $CoFe_2O4$ nanoplates [66]. This too suggests higher catalytic activity and favorable kinetics for mesoporous spinel oxides compared with bulk materials.

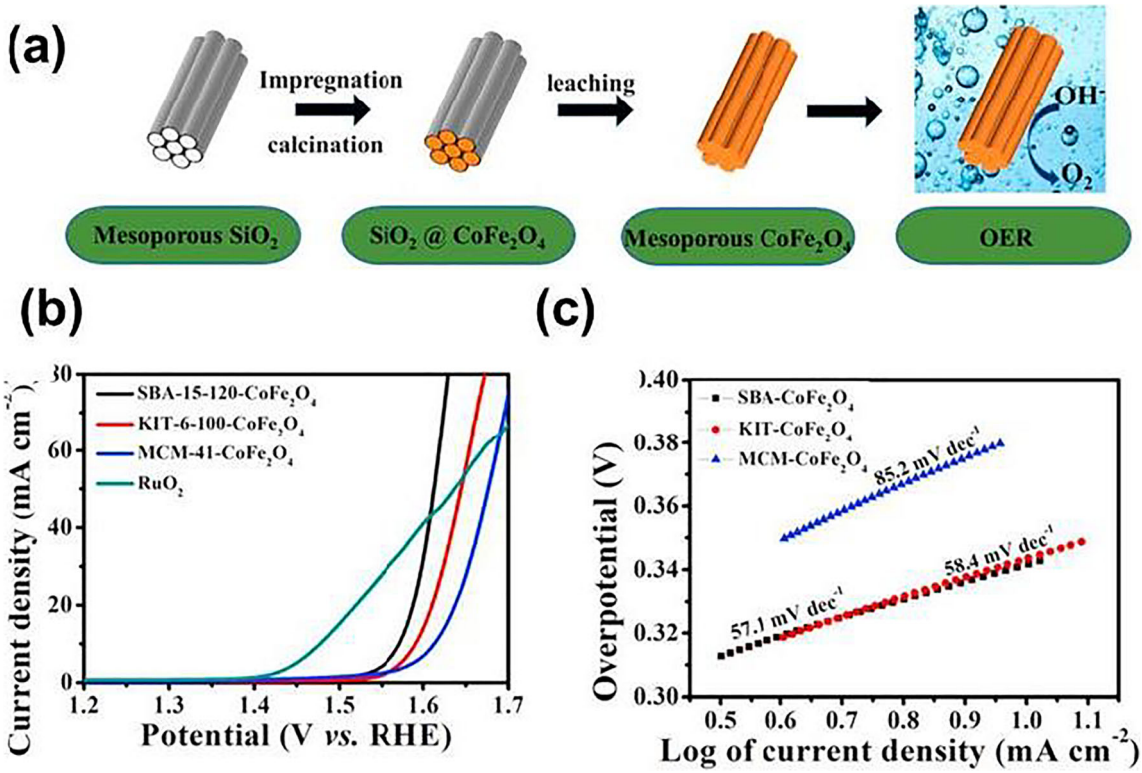

Fig. 5 **a** Illustration of the nanocasting approach for the preparation of mesoporous spinel $CoFe_2O_4$ catalyst replicated from 2D hexagonally SBA-15-120. **b** OER polarization curves and **c** their corresponding Tafel plots. Reproduced with permission from ref. [51]. Copyright 2019, Elsevier

Oxygen Reduction Electrocatalysis for Fuel Cell

Regenerative fuel cells (RFC) as a promising energy storage device require bifunctional oxygen electrocatalysts that are active for both oxygen evolution and reduction reactions. In the fuel cell field, conductive mesoporous materials, especially mesoporous carbon, have been intensively investigated to prepare electrocatalysts for electrodes, in order to overcome the challenge of cost and durability of the commercial Pt/C catalyst [67]. Thus, spinel (meso-Co_3O_4) templated using KIT-6 mesoporous silica are reported by Sa et al. [55]. These are highly active and stable bifunctional electrocatalysts. As we can see in Fig. 6, ordered mesoporous Co_3O_4 showed high activity for OER. The observed activity is found to be superior to Co_3O_4 NPs and comparable with Ir/C catalyst in an alkaline medium (0.1 M KOH). In addition to the promising activity and fast kinetics for ORR, mesoporous Co_3O_4 possesses superior methanol tolerance with a total overpotential of 1.03 V for OER (at 10 mA cm^{-2}) and ORR (at 3 mA cm^{-2}). These values are superior to the Pt/C benchmark catalyst. This is attributed to the structural stability of the mesoporous Co_3O_4 catalysts and its high surface area. Furthermore, in order to investigate the effect of the incorporation of non-platinum, earth-abundant metals, recently Behnken et al. reported the synthesis of mesoporous spinel phase Co_3O_4, $NiCo_2O_4$, and $CuCo_2O_4$ [68]. The presence of Ni^{2+} and Cu^{2+} materials made using KIT-6 template has uniform morphology and high specific surface areas (≈ 100 m^2g^{-1}). This led to enhancement in the ORR activity. It is believed that the enhancement of the ORR activity is due to the additional active sites as compared with mesoporous Co_3O_4 pristine.

Rechargeable Batteries

Rechargeable batteries are widely used in consumer electronics and electrical vehicles and are the prime candidates for grid energy storage [69]. Nanocasting synthesis pathway can produce hierarchical porous materials that have properties particularly useful in batteries. The mesoporosity in the electrode can boost the transport properties of electrolytes and improve rate and cycling performance. Until now, a variety of nanocasting cobalt-based metal oxide electrodes with diverse structures and morphologies have been synthesized and used as lithium-ion batteries (LIBs), sodium-ion batteries (SIBs), Zn-based batteries (ZBBs), and lithium–oxygen batteries. Table 2 summarizes different nanocasting cobalt-based mesoporous materials for batteries.

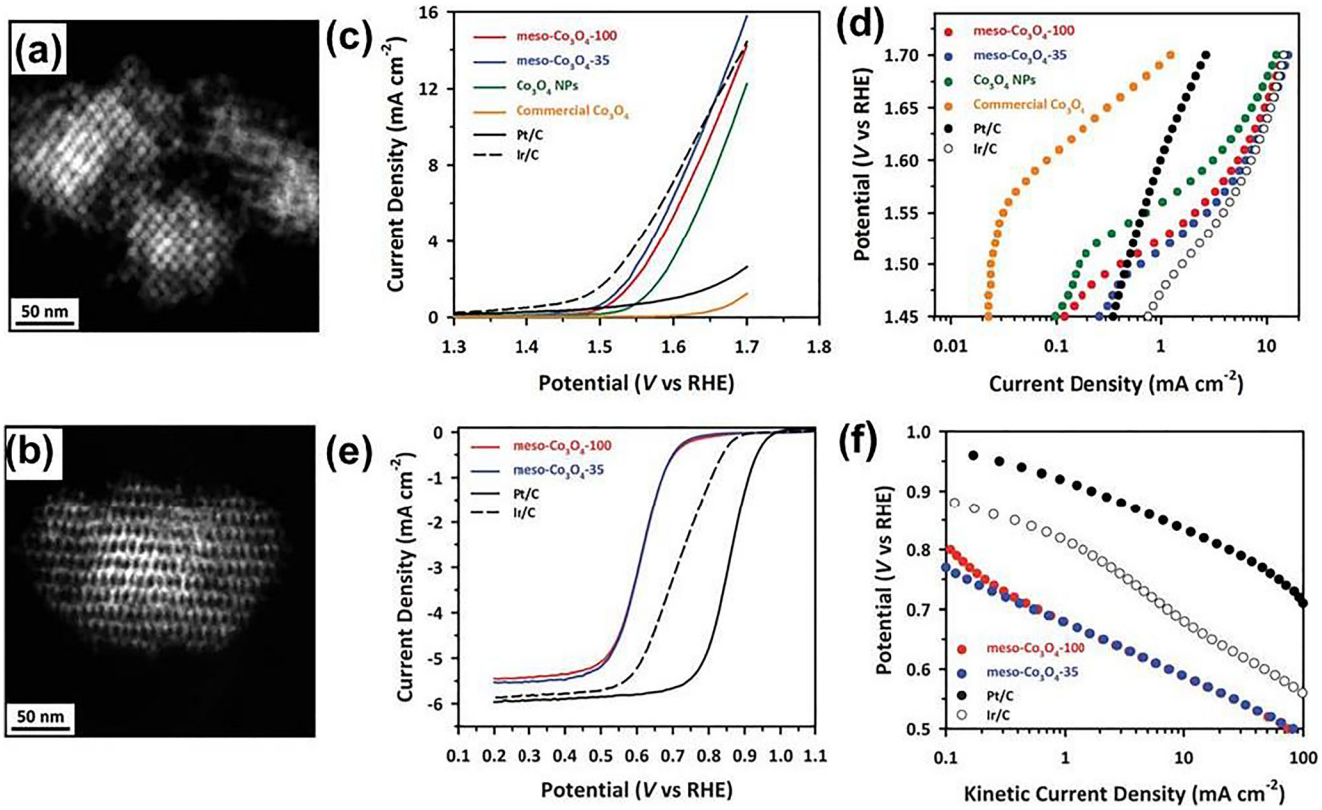

Fig. 6 **a** Darkfield TEM images of mesoporous-Co_3O_4-100 and **b** mesoporous-Co_3O_4-35. **c** OER polarization curves and **d** the corresponding Tafel plots for meso-Co_3O_4-100, mesoporous-Co_3O_4-35, Co_3O_4 NPs, commercial Co_{3O4}, Ir/C, and Pt/C catalysts in 0.1 M KOH solution. **e** ORR polarization curves and **f** the corresponding Tafel plots for mesoporous-Co_3O_4-100, mesoporous-Co_3O_4-35, Ir/C, and Pt/C catalysts. Reproduced with permission from ref. [55]. Copyright 2013, Royal Society of Chemistry

Lithium-Ion Batteries

In commercial LIBs, carbons and lithium metal oxides are commonly employed as the negative and positive electrode materials, respectively [83]. Through the application of nanotechnology, the size and the morphology of the Li-ion battery electrode architectures of both anode and cathode can be enhanced for achieving next-generation electrochemical energy storage devices [84, 85]. In fact, mesoporous lithium intercalation compound materials with regular porosity promote facile and fast Li-ion diffusion in which it can deliver higher rate capabilities and high stability compared with bulk electrode [86–89] The discovery of reversible conversion reactions, $Co_3O_4 + 8Li^+ + 8e^- \rightarrow 4Li_2O + 3Co$, with highest capacity at least on the initial discharge of 890 $mAhg^{-1}$ [90]. Such results showcase promise for achieving further improvements in the development of anodes for rechargeable lithium batteries [91].

Jiao et al. report earlier that the 2D nanowire and 3D cubic mesoporous $LiCoO_2$ replicated from SBA-15 and KIT-6 hard templates are effective anode materials for rechargeable lithium batteries [41]. The synthesis involves, first, preparation of mesoporous or nanowire Co_3O_4. This is followed by template removal, and the reaction of Co_3O_4 with LiOH at 400 °C for 1 h. Preliminary electrochemical data demonstrate that the nanostructured materials obtained thus with highly crystalline structures exhibit superior capacity retention on cycling compared with bulk $LiCoO_2$. Through the change of the hydrothermal treatment temperature, other forms of ordered mesoporous Co_3O_4 are also prepared and demonstrated to exhibit favorable electrochemical performance. The larger pores provide an efficient transport for Li ions, while the smaller pores offer large electrochemically active areas [70]. As illustrated in (Fig. 7 a and b) Park et al. reported nanostructural changes upon volume expansion of nanocasting Co_3O_4 during charge–discharge process using small-angle X-ray scattering characterization. They prove the role of mesopores in the performance of the active materials during electrochemical process. The mesopores in fact help to effectively accommodate the volume expansion of crystalline frameworks by the reaction with lithium [86]. Recently, Ette et al. [76] reported the synthesis of ordered mesoporous Co_3O_4 via unidirectional hexagonal MCM-41 and three-dimensional cubic MCM-48 silica templates. This material is then used as an anode for lithium-ion battery. Mesoporous Co_3O_4 show high initial reversible capacities (75% Coulombic efficiency), excellent electrochemical cycling stability, and enhanced rate performance. In the first cycle, unidirectional hexagonal M1-Co_3O_4 delivers

Table 2 Electrochemical performance of nanocasting cobalt-based mesoporous metal materials for batteries

Samples	Electrode	Current density (mA g^{-1})	1st discharge capacity (mAh g^{-1})	Capacity upon cycling (mAh g^{-1})	CE[a]	CN[b]	Refs.
Lithium-ion batteries							
Co_3O_4-KIT-6-40	Anode	50	1489	1141	95	25	[70]
Co_3O_4-KIT-6-80	Anode	50	1352	1140	67.9–91.1	25	[70]
Co_3O_4-KIT-6-100	Anode	50	995	943	67.9–91.1	25	[70]
Co_3O_4-KIT-6-130	Anode	50	989	1029	67.9–91.1	25	[70]
Co_3O_4-SBA-15-100	Anode	50	852	774	67.9–91.1	25	[70]
m-$CuCo_2O_4$-40	Anode	60	1564	1080	69	6	[71]
m-$CuCo_2O_4$-130	Anode	60	1401	829	59	6	[71]
HOM-$ZnCo_2O_4$	Anode	2.0	1982.7	1623	76.4	200	[72]
NPS-$ZnCo_2O_4$	Anode	2.0	1624.6	1286	76.0	200	[72]
Meso-$Co_{0.5}Sn_{0.5}$	Anode	50	822	-	25	50	[73]
Meso-$Co_{0.3}Sn_{0.7}$	Anode	50	1321	637	69	50	[73]
Meso-$Co_{0.1}Sn_{0.9}$	Anode	50	1493	-	40	50	[73]
m-Co_3O_4-S1	Anode	-	1121.8	-	> 80	5	[74]
$NiCo_2O_4$	Anode	100	1467	430	> 95	50	[75]
M1-Co_3O_4	Anode	890	1315	1190	75	100	[76]
M8-Co_3O_4	Anode	890	1530	790	75	100	[76]
$LiCoO_2$	Anode	30	20	20	55	50	[41]
Sodium-ion batteries							
Dual-meso Co_3O_4	Anode	90 810 2430	707	416 357 267	- - -	100	[77]
Zn-based batteries							
M-Co_3O_{4-x}	Cathode	1.0	384	420	-	50	[78]
M-Co_3O_4	Cathode	1.0	150	~ 150	-	50	[78]
Co_3O_{4-x}	Cathode	1.0	80	~ 80	-	50	[78]
Co_3O_4	Cathode	1.0	50	~ 50	-	50	[78]
Li–O_2/air batteries							
$CuCo_2O_4$	Cathode	100	500	~ 500	-	30	[79]
$NiCo_2O_4$	Cathode	-	4357	-	65.4	5	[80]
$NiCoMnO_4$	Cathode	30	137	100	72	400	[81]
$ZnCo_2O_4$	Cathode	100	6024	-	-	40	[82]

[a] CE, Coulombic efficiency

[b]Cycle number

a discharge capacity of 1190 mAh g^{-1}. On the other hand, three-dimensional cubic M8-Co_3O_4 exhibits 790 mAh g^{-1} after 100 charge–discharge cycles. The excellent electrochemical Li-ion storage of mesoporous Co_3O_4 is due to the unique mesoporous architecture this material has that provides shorter ionic diffusion paths and enhanced electrolyte percolation [86].

Cobalt spinel oxides with the general AB_2X_4 formula have generated intense interest for lithium-ion batteries. Among them, the $ZnCo_2O_4$ structure is consistent with that of the Co_3O_4 crystal; here Zn^{2+} ions replace Co^{2+}. Highly ordered mesoporous spinel HOM-$ZnCo_2O_4$ with controlled morphology and narrow pore size distribution is reported by Zhao et al. (Fig. 7c). When used as an anode material in rechargeable lithium-ion batteries, the resultant HOM-$ZnCo_2O_4$ (replicated from SBA-15) shows a high reversible specific capacity (up to 1623 mAh g^{-1}) which is greater than 1286 mAh g^{-1} observed for NPS-$ZnCo_2O_4$ (replicated from silicon spheres) at a current density of 2.0 A g^{-1}. Besides, HOM-$ZnCo_2O_4$ exhibited a higher capacity of 1470 mAh g^{-1} at a high current density of 8.0 A g^{-1} [11].

The effect of mesostructural regularity on lithium-ion battery has been evaluated by the Sun group [71]. In their work, mesoporous crystalline $CuCo_2O_4$ with coupled and uncoupled sub-structure was synthesized via a nanocasting strategy using mesoporous silica KIT-6-130 and KIT-6-40, respectively. It

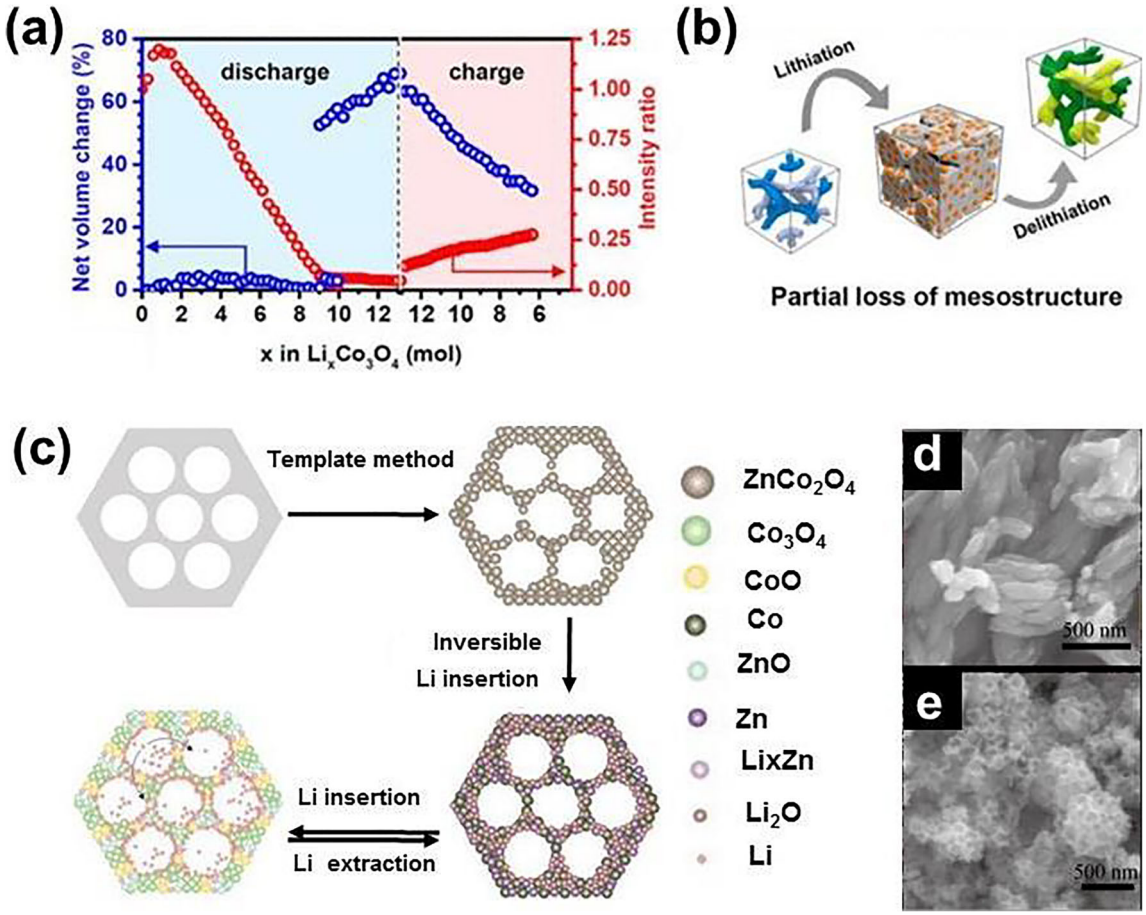

Fig. 7 **a** Net volume change and intensity ratio with contained lithium in the mesoporous Co_3O_4 electrode material for the initial lithiation–delithiation. **b** Schematic illustration of pore dynamics with respect to lithium-storage reaction reproduced with permission from ref. [86]. Copyright 2015, American Chemical Society. **c** Schematic illustration of the lithium insertion–extraction mechanism for the hexagonally ordered mesoporous $ZnCo_2O_4$ (HOM-$ZnCo_2O_4$) samples. **d** FESEM images of HOM-$ZnCo_2O_4$ and **c** NPS-$ZnCo_2O_4$. Reproduced with permission from ref. [72]. Copyright 2016, Elsevier

was found that uncoupled mesoporous $CuCo_2O_4$ shows better Li-storage performance than the coupled mesoporous $CuCo_2O_4$, delivering an initial discharge capacity of 1564 mAh g^{-1} and a reversible capacity of 900 mAh g^{-1} after the 6th cycle. More recently, Wu and coworkers [75] reported highly mesoporous microsphere spinel $NiCo_2O_4$ with large surface area (~ 97.77 m^2g^{-1}) and uniform pore size distribution. Compared with their bulk counterparts, $NiCo_2O_4$ excellent Li-storage electrode with an initial discharge capacity of ~ 1.467 mAh g^{-1} at a current density of 100 mAg^{-1}. It has been claimed that a highly ordered mesoporous structure could increase active sites and improve ion transport in the electrolyte/electrode interface.

Sodium-Ion Batteries

Sodium-ion batteries (SIBs) have been explored as one of the reasonable alternatives to LIBs due to limited lithium sources. This is in contrast with the abundant and wide distribution of sodium resources [92]. $NiCo_2O_4$ spinel oxide with an initial discharge capacity of ~ 618 mAh g^{-1} was the first reported metal oxide as an anode electrode for SIBs in 2002 [93]. However, during sodiation and desodiation, the large available surface area can improve the electronic contact between active materials, avoid aggregation, and facilitate the mass transport of electrolyte. In this context, Yang and coworkers [77] reported the synthesis of ordered mesoporous Co_3O_4 (m-Co_3O_4) through nanocasting. These materials have been investigated as an electroactive anode material in a sodium-ion battery. Ordered mesoporous Co_3O_4 replicated from KIT-6 exhibited an appreciable initial capacity of 707 mAh g^{-1} at a current density of 90 mA g^{-1}. Moreover, 3D mesoporous Co_3O_4 retains a capacity of 416 mAh g^{-1} after 100 cycles providing much better transport than the bulk Co_3O_4 material. It is considered that the nanostructure provides a large electrode–electrolyte interface for electrolyte adsorption. This facilitates the mass transport of electrolyte in larger pores and sodium-ion diffusion in smaller pores [77]. To explain the sodiation/desodiation mechanism, they revealed that during the first discharge, sodium ions were inserted into m-Co_3O_4 by surface

reconstruction reactions to form $Na_xCo_yO_z$, which is then partially transformed into Co_xO and Na_2O accompanied by surface amorphization through further sodiation. The ex situ XRD analysis confirmed the occurrence of reversible conversion reaction during the uptake/extraction of sodium ions.

Li–O_2/Air Batteries

Li–O_2 batteries are composed of porous oxygen diffusion cathode, a Li-ion conducting nonaqueous electrolyte, and Li metal as the negative electrode. The oxygen is reduced in pores of the positive electrode and then combined with the Li ions to form Li_2O_2 ($O_2 + 2Li^+ + 2e^- \leftrightarrow Li_2O_2$). It has been proved that cobalt-based oxides exhibit a high affinity with Li_2O_2 and promote its electrochemical oxidation. This plays an important role in enhancing the cycling performance [94]. However, the mesostructures are an important characteristic feature of this class of electrodes in batteries due to their influence on mass transfer and adsorption properties. Based on the above considerations, Li et al [80]. reported 3D ordered mesoporous $NiCo_2O_4$ as a bifunctional electrocatalyst for Li–O_2 batteries. Mesoporous catalyst is prepared employing the nanocasting method using KIT-6 as a template and Co and Ni nitrates as precursors. The resulting material has a relatively high BET surface area of ~ 95.5 $m^2\ g^{-1}$, which is then tested as a bifunctional catalyst towards both ORR and OER. When compared with the classical carbon electrode, higher current densities, lower OER, and higher ORR onset potentials are obtained for most mesoporous $NiCo_2O_4$ carbon electrodes. Moreover, employing 3D mesoporous $NiCo_2O_4$ as cathode for Li–O_2 batteries exhibited a high specific capacity of 4120 mAh g^{-1} and a promising capacity retention rate after 5 cycles of 65.4%. The Li group reported similar research on 3D ordered mesoporous $ZnCo_2O_4$ [82]. Compared with pure carbon, the Li–O_2 batteries employing mesoporous $ZnCo_2O_4$ as cathode possess a higher specific capacity of 6024, 3710, 3119, and 1674 mAh g^{-1} at current rates of 100, 200, 500, and 1000 mA g^{-1}, respectively. In this direction, 3D mesoporous $CuCo_2O_4$ with a specific surface area of 97.1 $m^2\ g^{-1}$ has been also reported by the same group [79]. In comparison with pure carbon electrode, 3D mesoporous $CuCo_2O_4$ shows a lower anodic onset potential a higher cathodic peak voltage and higher current densities. The Li–O_2 batteries employing mesoporous $CuCo_2O_4$ as cathode possess a high specific capacity of ~ 7456 mAh g^{-1} and enhanced cyclability at 100 mA g^{-1} current rate.

Zinc-Based Batteries

Aqueous zinc-based batteries (ZBBs) have been considered attractive as energy storage system due to the substantial abundance of Zn on earth compared with lithium.

Owing to high theoretical capacity (446 mAh g^{-1}), low-cost, earth abundance, and high thermodynamic stability, cobalt oxide (Co_3O_4) has received interest as a promising ZBB cathode material [95]. Recently, Teng et al [78]. reported the synthesis of 3D ordered mesoporous cobaltosic oxide (M-Co_3O_4) with rich oxygen vacancies (M-Co_3O_{4-x}) as the durable cathode for Zn-based batteries. As shown in Fig. 8, M-Co_3O_{4-x} is prepared through a simple nanocasting method; subsequently, thermal-reduction is carried out to create oxygen vacancies within the metal oxide. The resulting M-Co_3O_{4-x} exhibits a remarkable capacity of 384 mAh g^{-1} at 1.0 A g^{-1} which is greater than that of the pristine Co_3O_4//Zn battery (50 mAh g^{-1}). The enhancement of energy storage capacity is attributed to unique mesoporous architectures, an abundance of active sites, and more importantly the synergistic effect of mesopores and oxygen vacancies. This is confirmed further by DFT calculations [78]. Moreover, M-Co_3O_{4-x}//Zn battery exhibits extraordinary cycling stability, capacity after 60,000 cycles [78].

Supercapacitors

Unlike common batteries, electrochemical capacitors are promising energy storage systems due to their larger power density, rapid charging–discharging, and longer cycle life [96–98]. A range of nanocast mesoporous cobalt oxides has been used as supercapacitors devices.

Zheng and coworkers [99] demonstrate that nanocasting strategy is one of the diverse routes to generate mesoporous supercapacitor electrodes by the synthesis of mesoporous Co_3O_4 replicated from different parent structures and at different calcination temperatures. Electrochemical tests show that specific capacitance of the samples decreases slightly with the increase of their calcination temperature. However, the nature of mesostructure (2D hexagonal or 3D *Ia3d* cubic structure) does not obviously affect the specific capacitance value of the samples. An and coworkers [100] reports the synthesis of highly ordered mesoporous spinel $NiCo_2O_4$ by a hard template and subsequently examine its electrochemical performance. On the basis of their report, *Ia3d* cubic mesoporous $NiCo_2O_4$ replicated from KIT-6 as a parent template shows an exceptionally high specific capacitance (1699 F g^{-1} at a current density of 1 A g^{-1}) and an excellent cycling ability (~ 104.1% retention after 10,000 cycles). More recently, mesoporous $CuCo_2O_4$ nanowire arrays are prepared through nanocasting from a silica SBA-15 template (Fig. 9) [101]. In addition to their highly ordered mesostructures, nanocasted mesoporous $CuCo_2O_4$ exhibits superior pseudocapacitance of 1210 F g^{-1} in the initial cycles at a current density of 2 A g^{-1}. After electroactivation of the electrode in the subsequent 250 cycles, the capacitance increases to 3080 F g^{-1}. Hence, the asymmetric supercapacitor device designed by the mesoporous $CuCo_2O_4$ nanowires as a positive electrode and activated carbon as a negative electrode demonstrates a high energy density of 42.8 Wh kg^{-1} much higher

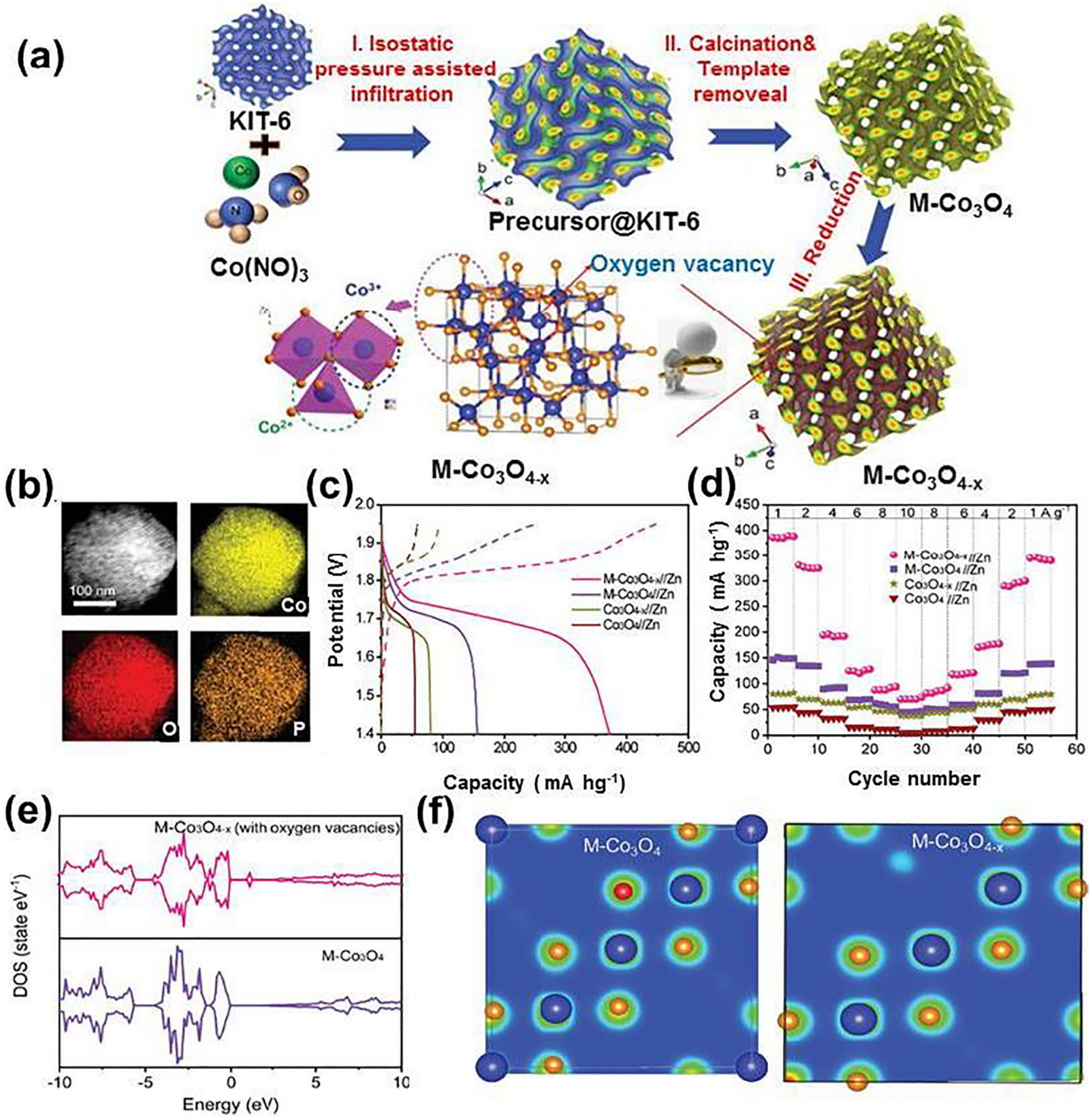

Fig. 8 Schematic representation of the procedure used in the preparation of mesoporous M-Co_3O_4 and M-Co_3O_{4-x} samples. **b** HAADF-STEM of M-Co_3O_{4-x} and its corresponding elemental color mapping for Co, O, and P. **c** Charge/discharge curves at 10 mV s^{-1} and 1 A g^{-1} and **d** the rate capability curves at various current densities of the M-Co_3O_{4-x}//Zn, M-Co_3O_4//Zn, Co_3O_4-x//Zn, and Co_3O_4//Zn batteries. **e** Density of states of mesoporous M-Co_3O_4 pristine and M-Co_3O_4-x (with oxygen vacancies). **f** The differential charge density of M-Co_3O_4 and MCo_3O_{4-x}. Reproduced with permission from ref. [78]. Copyright 2019, Royal Society of Chemistry

than most of the reported asymmetric aqueous supercapacitors.

Other Related Energy Applications

Hydrogen generated from water in the presence of sunlight is another promising source of clean and renewable energy [102]. The Rosen group reported nanocasting mesoporous Mg-Co_3O_4 with an ultrahigh surface area (≈ 250 m^2g^{-1}) which exhibits high oxygen evolution activities in both the visible light-driven $[Ru(bpy)_3]^{2+}$ persulfate system and the Ce^{4+}/Ce^{3+} chemical water oxidation system [103]. The same group further proved the importance of the octahedral sites in the cobalt spinel structure for photocatalytic oxygen

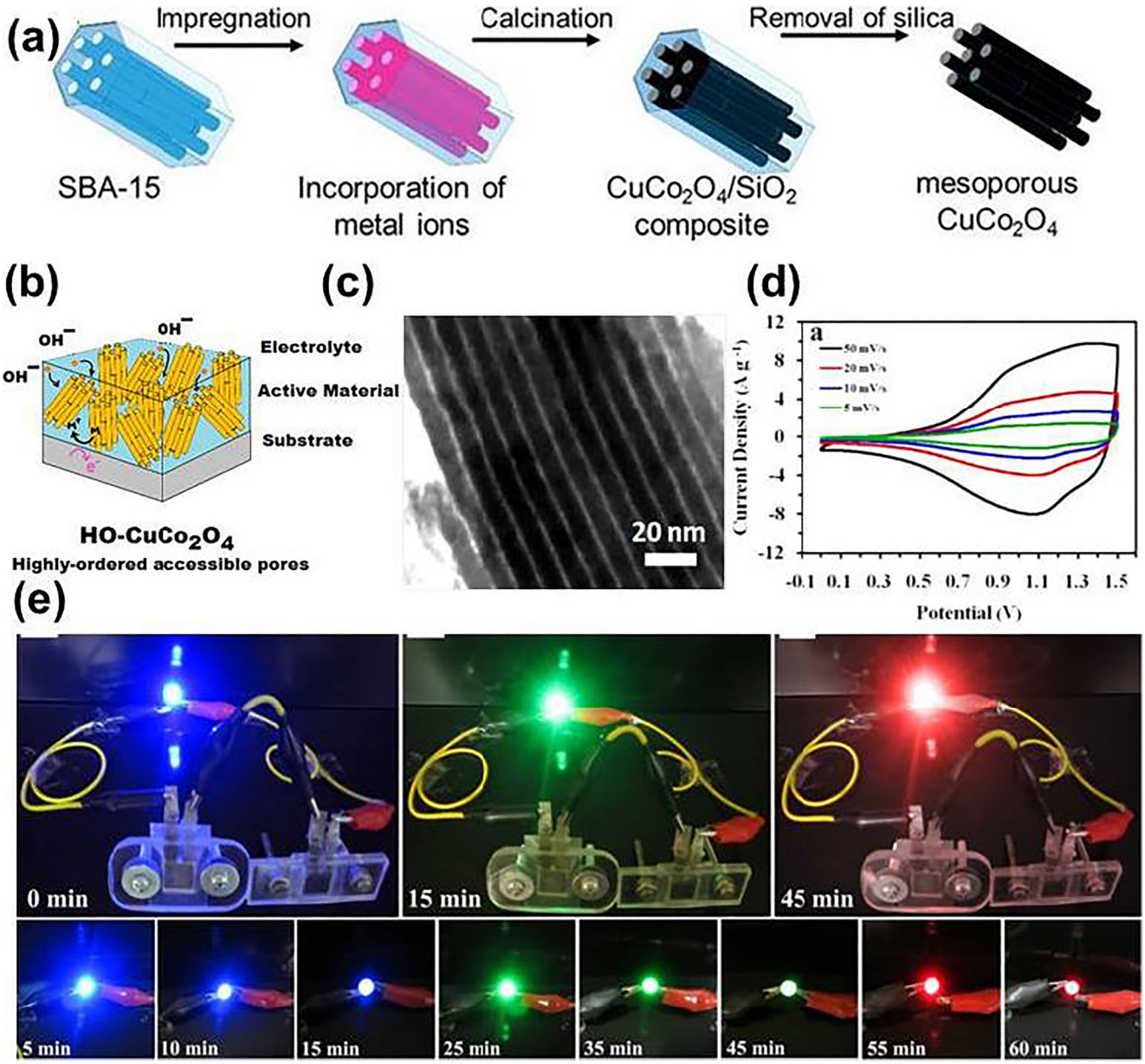

Fig. 9 **a** Schematic preparation steps of two-dimensionally mesoporous $CuCo_2O_4$ nanowires via nanocasting from a KIT-6 template. **b** Schematic illustration of pore accessibility in the highly ordered $CuCo_2O_4$ (HO–$CuCo_2O_4$). **c** TEM images of $CuCo_2O_4$ nanowires. **d** CVs for the HO–$CuCo_2O_4$//AC asymmetric supercapacitor. **e** Photographs showing two supercapacitors in series which can light up blue, green, and red LED indicators, respectively, during 60 min. Reproduced with permission from ref. [101]. Copyright 2015, American Chemical Society

evolution. Ordered mesoporous cobalt oxides are doped with Ni, Mn, and Mg to realize relevant catalysts. The photocatalytic results show a difference in the oxygen evolution activities of metal in a Me_4O_4 cubane following this order: Co^{3+} > $Mn^{3.7+}$>> > $Ni^{3.3+}$ = Mg^{2+} [104]. In this context, Deng et al. [105] reported the synthesis of a series of Co_3O_4 templated using mesoporous SiO_2 nanospheres by changing the calcination temperature (from 150 to 750 °C) as photochemical water oxidation in a $[Ru(bpy)_3]^{2+}$ $[S_2O_8]^{2-}$ system. It is found that the O_2 production decreased with increasing calcination temperature. The nanostructured Co_3O_4 calcinated at low temperature (150 °C) exhibits the high photochemical water oxidation activity. Besides, mesoporous CoO with a similar nanoarchitecture synthesized using ethanol reduction shows a high turnover-frequency number for photochemical water oxidation of 4.1×10^{-4}. This is greater to 2.9×10^{-4} observed for mesoporous Co_3O_4-150 [105].

CO hydrogenation to valuable and clean synthetic liquid fuels through Fischer–Tropsch synthesis (FTS) is one of the promising chemical processes for green energy [[106, 107]. The cobalt-based FTS catalysts have been generally known to favorably produce higher molecular weight hydrocarbons

[108]. In the work of Ahn et al., three-dimensionally ordered mesoporous Co_3O_4 modified with Al_2O_3 demonstrated a stable and superior catalytic activity for CO hydrogenation into linear hydrocarbons. The enhanced catalytic stability is attributed to mesoporous channel architecture which enhances the transport rate of hydrocarbons formed during FTS reaction. Recently, 3% of phosphorous-modified m-CoAl (Co_3O_4–Al_2O_3) was prepared employing the nanocasting method using a hard template of KIT-6. The material obtained thus has enhanced catalytic activity for CO hydrogenation to hydrocarbons. It also has improved structural stability. The observed performance is explained using possible phase transformations of cobalt and aluminum species [109]. Additionally, nanocasting cobalt oxide has been used in CO_2 hydrogenation for conversion to valuable compounds (e.g., methane from CO_2 through $CO_2 + 4H_2 = CH_4 + 2H_2O$) [110]. Ordered meso-$ZnCo_2O_4$ nanospheres synthesized using a nanocasting method serves as non-enzymatic electrodes in H_2O_2 sensors and glucose biofuel cells (GBFCs). In the H_2O_2 sensor, meso-$ZnCo_2O_4$ achieves higher sensitivity (658.92 μA mM^{-1} cm^{-2}) with quick response time (5.2 s) compared with bulk $ZnCo_2O_4$. Moreover, as cathode material in GBFCs, mesoporous $ZnCo_2O_4$ possesses excellent open-circuit voltage of 0.83 V, the maximum power density of 0.32 mW cm^{-2}, and limiting current density of 1.32 mA cm^{-2} [111].

Nanocasting Mesoporous Cobalt-Based Derivates

Perovskites

Perovskite oxides possess a general formula of ABO_3, where A is a rare-earth or alkaline-earth metal and B is a transition metal [112]. One of the advantages of perovskite structures is the possibility to adopt a wide range of different compositions, changing either the A or the B cation or partially substituting cation(s) of the same or different valence. This results in the general formula $A_{1-x}A'_xB_{1-y}B_yO_{3\pm\delta}$ [113]. Mesoporous Co-based perovskite has been synthesized through the nanocasting pathway and is used for electrocatalysis reactions, carbon/nitrogen oxidation, and methane combustion (Table 3).

Recently, hierarchically ordered mesoporous $LaCoO_3$ was reported using the nanocasting method using SBA-15 as a hard template [117]. The resultant material has been applied as a bifunctional catalyst for both oxygen reduction and evolution reactions in 4 M KOH and 0.1 M CH_3COOK. The cell performance of a bifunctional electrode containing the highly porous $LaCoO_3$ catalyst is 14–44% higher than that of a conventional $LaCoO_3$ catalyst prepared using the sol–gel method. Besides, mesoporous $LaCoO_3$ showed stable cycle performance for charge and discharge at 20 mA cm^{-2} until 300 h [117].

Phosphides

Transition metal phosphide (TMPs) materials have recently been widely researched as electrocatalysts due to their desirable electronic, redox, and magnetic properties [118]. Meanwhile, the morphologies of TMPs demonstrate an attractive strategy for enhancing the electrocatalytic activity [19]. Among them, nanostructured Co-based phosphides could provide a much higher specific surface area and expose more active sites as compared with their bulk counterparts. Hard templating is one of the most suitable approaches for transition metal phosphide (TMPs) synthesis which offers accessible active sites, leading to easy mass/charge transfer [119]. Fu and co-authors, in 2016, reported the first synthesis of a family of three-dimensionally Co–Ni phosphides through nanocasting approach with large mesopores (8 nm) and controllable composition (Fig. 10a). After impregnation of nitrate precursors into the KIT-6 hard template and annealing, the obtained product is mixed with NaH_2PO_2 for phosphorization under the N_2 atmosphere. This is followed by the removal of silica templates. The resulting CoNiP nanocatalysts show superior catalytic activity and long-term stability towards the OER in alkaline solution. The optimized composition mesoporous Co_3Ni_1P possesses a low potential of 1.511 V at a current density of 10 mA cm^{-2} which is much lower than that of the 1.56 V and 1.56 for NiCoP/C nanoboxes and NiCoP/C nanoboxes, respectively [121]. This material in fact outperforms mesoporous CoP, NiP, and benchmark RuO_2 (Fig. 10b). The enhanced electrocatalytic performance has been attributed to the mesostructure associated with the material which provides a combination of abundant active sites, synergy between metals, and in situ formation of oxidized phosphates as active species [18].

The sensitivity of the metal phosphide composition towards HF and/or NaOH which are necessary for template removal paved the way for the removal of the template before the phosphorization process. In 2017, Yamauchi and coworkers synthesized ordered mesoporous cobalt phosphide (meso-CoP and meso Co_2P) through the gas–solid reaction of hexagonally mesoporous cobalt oxide replicated from SBA-15 with NaH_2PO_2 as the phosphorus source [122]. The electrocatalytic performances towards the oxygen evolution reaction of mesoporous are evaluated recently by the same group [120]. Due to its well-developed mesoporous architecture, meso-CoP exhibits a low overpotential of 0.30 V at a current density of 10 mA cm^{-2} with a smaller Tafel slope of 81 mV dec^{-1} (Fig. 10 e and f) and good long-term stability. The sample performs better than its bulk counterpart (0.336 mV) and most of the other reports on cobalt phosphides.

Table 3 Summary of cobalt-based porous perovskites prepared from hard-templating methods

Material	Template	BET surface area ($m^2\ g^{-1}$)	Catalytic application	Refs.
$LaCoO_3$	Mesoporous silica (KIT-6)	270	Oxygen reduction reaction	[15]
$LaFe_xCo_{1-x}O_3$	Mesoporous silica (KIT-6)	118–163	Oxygen reduction reaction	[15]
$Ba_{0.5}Sr_{0.5}Co_{0.8}Fe_{0.2}O_{3-\delta}$	Tetraethoxysilane (TEOS)	32.1	Oxygen evolution reaction	[52]
$LaCoO_3$	Mesoporous silica (KIT-6)	270	CO and NO oxidations	[114]
$LaFe_{0.6}Co_{0.4}O_3$	Carbon	30	Oxidation of CO to CO_2	[115]
$LaCoO_3$	Mesoporous silica KIT-6	96.7	Methane combustion	[116]
$LaCoO_3$	Mesoporous silica SBA-15	15.6–62.6	Oxygen reduction/evolution	[117]

In addition to their good electrocatalytic proprieties towards oxygen evolution, it has been widely accepted that P atoms in cobalt phosphide play a pivotal role in the hydrogen evolution reaction [123]. Through a simple nanocasting using KIT-6 as a hard template, more recently, Huang and co-workers [124] reported 3D mesoporous cobalt ferrite

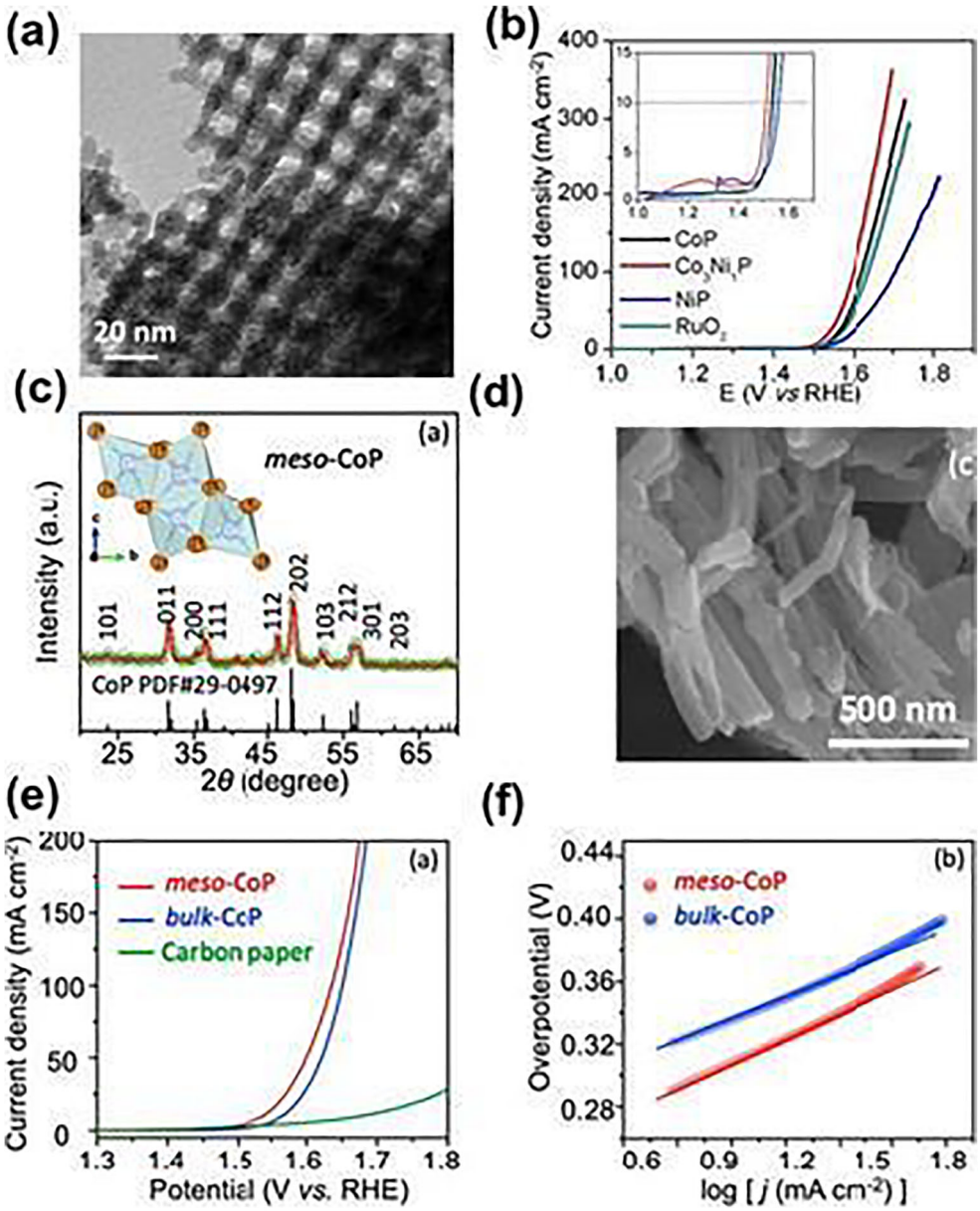

Fig. 10 **a** TEM images of mesoporous CoP, NiP, and Co_3Ni_1P. **b** LSV polarization curves of mesoporous CoP, Co_3Ni_1P, NiP, and RuO_2 at 1600 rpm in O_2-saturated 1 M KOH. Reproduced with permission from ref. [18]. Copyright 2016, American Chemical Society. **c** XRD patterns with crystal structure models of mesoporous cobalt phosphide (*meso*-CoP). **d** SEM images of *meso*-CoP. **e** Polarization curves and **f** the corresponding Tafel plots of *meso*-CoP and bulk-CoP in 1 M KOH solution with a scan rate of 5 mV s^{-1}. **e** Durability test and **f** time-dependent current density curve of *meso*-CoP under a static overpotential of 390 mV in 1 M KOH solution. Reproduced with permission from ref. [120]. Copyright 2019, Elsevier

phosphides $Co_{1-x}Fe_xP$ as a bifunctional catalyst for overall water splitting for both OER and HER. The optimized $Co_{0.75}Fe_{0.25}P$ with large surface area and accessible pore volume show superior performance with a very low overpotential of 270 and 209 mV at 10 mA cm^{-2}. The electrocatalyst in alkaline media offers good durability and long-time stability for both OER and HER. Additionally, the bifunctionality of mesoporous $Co_{0.75}Fe_{0.25}P$ allows it to be directly employed as both anode and cathode in an alkaline electrolyzer with a low cell voltage 1.63 V, yielding a current density of 10 mA cm^{-2} with outstanding stability for 18 h.

Nitrides

Unlike cobalt oxide/hydroxide compounds, cobalt nitride shows a similar metallic electrical conductivity and structural stability which would be beneficial to facilitate the redox reaction kinetics when used as an electrode material [125]. Therefore, the combination of ordered mesoporous structures with conductive metal nitride can further enhance ion/electron transportation, accelerate kinetics, and exhibit higher performance than the counterpart of bulk oxides. The first synthesis of mesoporous cobalt nitride through nanocasting was done for the first time by Shi and coworkers [43]. This can generally take one of two synthetic routes: (i) direct nitridation of mesoporous oxides or (ii) the transformation of mesostructured metal oxides/silica composites to nitrides/silica composites then removal of a template (Fig. 11a) [128]. Following the first route, recently, Jiang et al. reported three-dimensionally 3D interconnected cubic mesoporous CoN with ordered mesopores

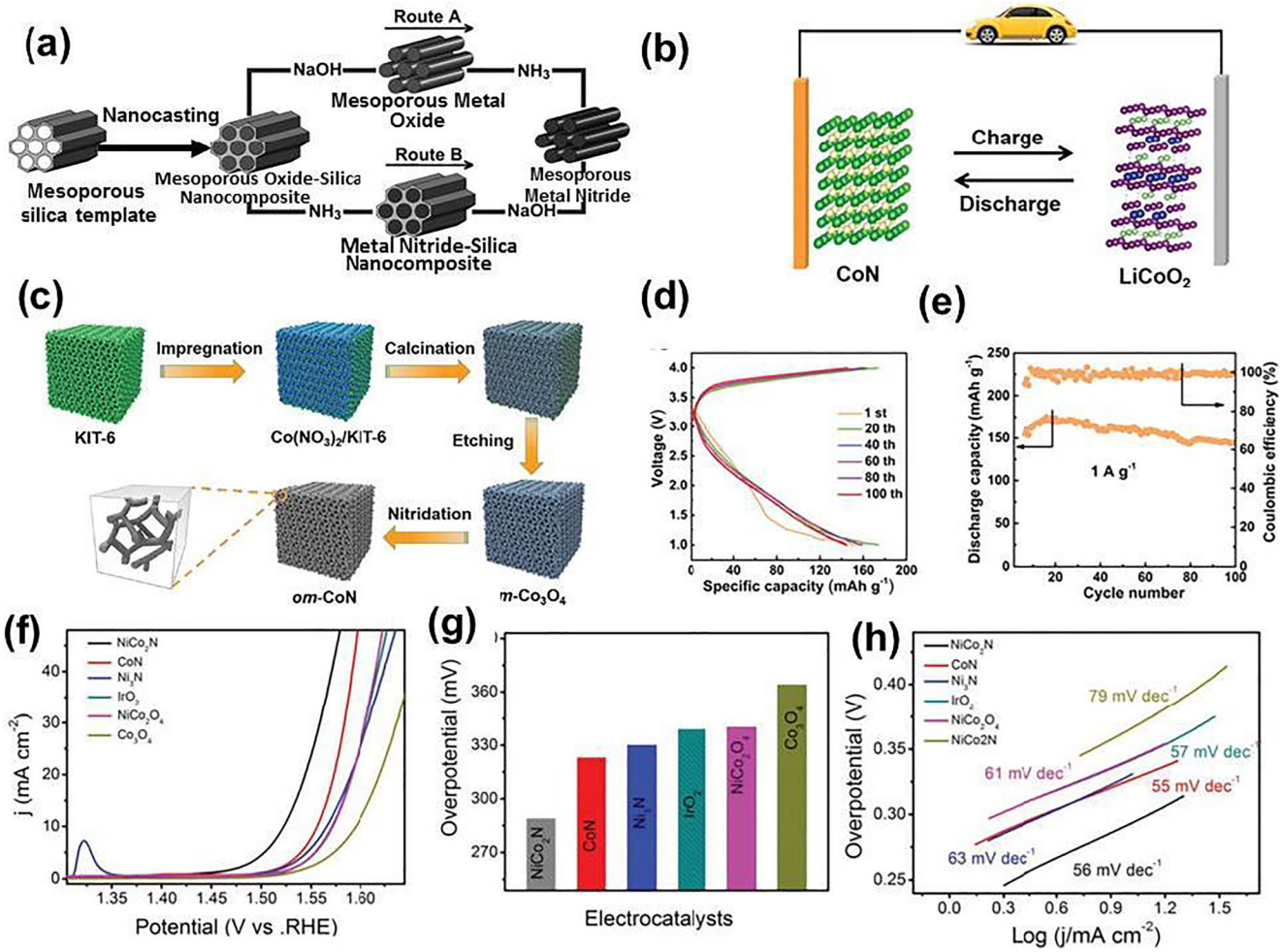

Fig. 11 **a** Schematic illustration of two nanocasting pathways for the synthesis of mesoporous nitrides. Reproduced with permission from ref. [43]. Copyright 2008, Wiley-VCH. **b** Schematic illustration of the preparation of mesoporous cobalt nitride (om-CoN). **c** Schematic illustration of the full lithium-ion battery with the om-CoN/$LiCoO_2$ couple; **d** galvanostatic charge and discharge profiles, **e** cycling performance of the full battery at 1 A g^{-1} for mesoporous cobalt nitride. Reproduced with permission from ref. [126]. Copyright 2019, Royal Society of Chemistry. **f** OERLSV polarization curves, **b** the corresponding overpotentials at a current density equal to 10 mA cm^{-1} and **c** Tafel plots for mesoporous Co_3O_4, $NiCo_2O_4$, IrO_2, CoN, and $NiCo_2N$. Reproduced with permission from ref. [127]. Copyright 2019, Wiley-VCH

(~ 7.5 nm) replicated from KIT-6 as lithium battery electrode [126]

Lithium-ion batteries are achieved using 3D CoN ordered mesoporous structures; this enhanced ion transportation capability and lithium diffusion. It is considered that mesoporous channels and conductive networks in mesoporous nitrides enable the rapid infiltrability/diffusion and rapid electron migration in lithium-ion batteries [129]. As a consequence, 3D interconnected cubic CoN delivered a large capacity, a high rate capability, and stable specific capacity of 710 mAh g^{-1} after 350 cycles at 1 A g^{-1} which is greater than previously reported CoN LIB electrodes. Besides, designing lithium-ion full cells using the mesoporous CoN as cathode and $LiCoO_2$ (LCO) as the anode (Fig. 11c) demonstrates a high initial specific charge and discharge capacity of 175 and 150 mAh g^{-1}.

Cobalt nitrides have been reported as highly active OER catalysts. Nevertheless, doping of nickel into cobalt nitride compounds can enhance their overall electrochemical performance. Taking this into consideration, recently in our work, we reported the hard-templating pathway to synthesize 3D ordered mesoporous ternary nitrides $NiCo_2N$ from its corresponding mesoporous spinel $NiCo_2O_4$ using the mesoporous silica KIT-6 hard template [127]. Mesoporous ternary nitride $NiCo_2N$ demonstrates outstanding performance as oxygen evolution electrocatalyst with very low overpotential (289 mV) at a geometric current density of 10 mA cm^{-2} and a small Tafel slope (56 mV dec^{-1}). This is lower than the benchmark IrO_2 and that of mesoporous binary nitrides CoN and Ni_3N electrocatalysts (Fig. 11g). We attributed the superior activity to the intrinsically rich conductivity and high active electrocatalyst contact area.

Sulfides

Crystalline porous sulfides have taken on a significant role in various energy storage applications because they combine the interconnected porous networks, large quantity of surface metal site, and good conductivity in a better manner when compared with its counter oxides. A high-temperature reductive sulfuration approach reported by Shi et al. can be considered as the first effort to prepare highly ordered mesoporous metal sulfide crystallites by hard template [130]. As the first step, nanocasting generates metal precursor/mesoporous silica composites. H_2S gas is subsequently utilized as a sulfuration agent to in situ convert metal precursors to sulfides crystallites in the silica nanochannels. Upon etching, silica mesoporous sulfides are produced. Later, Yonemoto et al131 [131]. using a new synthetic approach represents an oxide-to-sulfide nanocasting method using H_2S gas as a sulfur source. This in fact yielded the first example of highly interconnected ordered mesoporous cobalt sulfide with a crystalline wall (Fig. 12a). However, using H_2S needs particular caution since it is poisonous and highly corrosive. In order to overcome this drawback, Jin and coworkers [133] reported the synthesis of

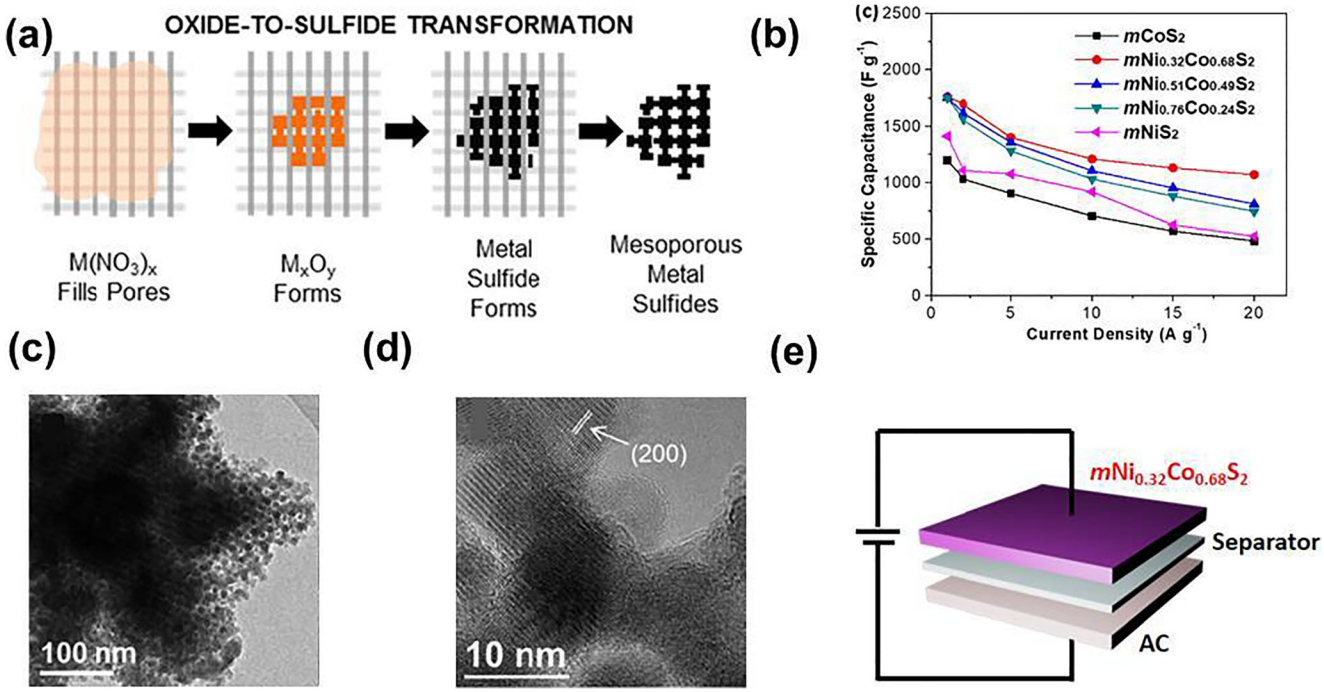

Fig. 12 **a** Schematic preparation steps of highly ordered mesoporous sulfides via oxide-to-sulfide approach. **b** TEM and **c** HRTEM images of mesoporous cubic Co_2S. Reproduced with permission from ref. [132]. Copyright 2014, American Chemical Society. **d** Specific capacitance of mesoporous ternary sulfides $Ni_xCo_{1-x}S_2$ at different current densities. **e** Schematic illustration asymmetric supercapacitor device based on mesoporous $Ni_{0.32}Co_{0.68}S_2$//AC. Reproduced with permission from ref. [131]. Copyright 2017, American Chemical Society

a series of highly ordered mesoporous $Ni_xCo_{1-x}S_2$ with 3D cubic mesostructure using sulfur powder as the sulfur source. The material was then used in a supercapacitor; the generated bicontinuous mesoporous $Ni_{0.32}Co_{0.68}S_2$ possesses a specific capacitance up to 1698 F g^{-1} at a current density of 2 A g^{-1}. This value is greater than those of CoS_2 and NiS_2 single mesoporous sulfides (Fig. 12b). Moreover, designing a hybrid asymmetric supercapacitor (ASC) device using $Ni_{0.32}Co_{0.68}S_2$ as the cathode, activated carbon (AC) as the anode and cellulose paper as the separator in a 2 M KOH (Fig. 12e). The device fabricated thus has a high energy density of 37 Wh kg^{-1} at a power density of 800 W kg^{-1}. This is comparable with the reported values obtained from metal sulfides [131].

Conclusions and Outlook

Over the past 5 years, several reports have appeared that indicate the promise of nanocasting cobalt-based mesoporous electrodes materials. This review summarizes the work thus far on nanocasting cobalt-based mesoporous materials including oxides and other materials (nitrides, phosphides, and sulfides) for energy-related technologies. In particular, the uses of these materials for electrocatalysis, rechargeable batteries, and supercapacitors have been explored. We show that high activity and stable electrochemical performance are achieved through morphology control and suitable design of electrode structure. The enhancement of the intrinsic activity of the active site can be tuned by electronic modulation of the electrocatalytically active centers. In addition, the use of a secondary phase including noble metals and other transition metals and varying the mixture of metals has been found to be helpful. The effect of nanostructuring design on chemical diffusion, charging/discharging, and cycling performance for rechargeable batteries is elaborated.

Despite recent progress discussed here, there are important challenges that need to be overcome to achieve the high-performance necessary for the state of the art electrochemical applications. The opportunities that exist are as follows: (i) in-depth investigations such in situ spectroscopy and theoretical calculations of the surface to better understand the correlations between the chemical composition, ion storage, and electrocatalysis; (ii) in supercapacitors and batteries, one may pursue a combination of high surface area and reactivity towards the energy storage; (iii) comprehensive and systematic studies may be carried out on cobalt-based mesoporous metal alloys and heterostructures [133]; (iv) it is necessary to establish the impact of mesostructure on long-term durability and cyclability; (v) last but not least, one can benefit from integrating these electrodes with controlled geometry and architectures directed towards viable, low-cost manufacturing method. Hence, there are prospects identified here are expected to help with furthering activity in electrochemically active materials that are realized via nanocasting.

Funding Information This work is supported by the Chinese Academy of Sciences (Grant No. 2018PS0011) and Natural Science Foundation of China (Grant No. 21471147 and 61971405) and the National Key Research and Development Plan (Grant No. 2016YFB0101205). M.Y. would like to thank the National "Thousand Youth Talents" program of China and Ningbo 3315 program for the support. T.T. acknowledges the funding from the Ministry of Electronics and Information Technology, India (Project ID: ELE1819353MEITNAK), and the Department of Science and Technology, India (Project ID: MET1617146DSTXTIJU, DST/TMD/MES/2K18/17, DST 11-IFA-PH-07, and DST/TMD/SERI/HUB/1(C), DST Solar Energy Harnessing Center, Materials for energy storage) for supporting this research work.

References

1. S. Ghosh, R.N. Basu, Nanoscale **10**, 11241–11280 (2018)
2. N. Hussain, F. Wu, L. Xu, Y. Qian, Nano Res **12**, 2941–2946 (2019)
3. N.M. Muresan, J. Willkomm, D. Mersch, Y. Vaynzof, E. Reisner, Angew. Chem. I nt. Ed. **51**, 12749–12753 (2012)
4. J. Tian, Q. Liu, A.M. Asiri, X. Sun, J. Am, Chem. Soc. **136**, 7587–7590 (2014)
5. S. Cobo, J. Heidkamp, P.A. Jacques, J. Fize, V. Fourmond, L. Guetaz, B. Jousselme, V. Ivanova, H. Dau, S. Palacin, M. Fontecave, Nat. Mater. **11**, 802 (2012)
6. K.K. Lee, W.S. Chin, C.H. Sow, J. Mater, Chem. A **2**, 17212–17248 (2014)
7. G. Wang, H. Liu, J. Horvat, B. Wang, S. Qiao, J. Park, H. Ahn, Chem.: Eur. J. **16**, 11020–11027 (2010)
8. B. Jiang, H. Song, Y. Kang, S. Wang, Q. Wang, X. Zhou, K. Kani, Y. Guo, J. Ye, H. Li, Y. Sakka, Chem. Sci. **11**, 791 (2020)
9. M.M. Nair, H. Yen, F. Kleitz, C. R. Chim. **1**, 641–655 (2014)
10. A.H. Lu, F. Schüth, Adv. Mater. **18**, 1793–1805 (2006)
11. F. Schuth, Angew. Chem. Int. Ed. **42**, 3604–3622 (2003)
12. J. Landon, E. Demeter, N. İnoğlu, C. Keturakis, I.E. Wachs, R. Vasić, A.I. Frenkel, J.R. Kitchin, ACS Catal. **2**, 1793–1801 (2012)
13. Y. Ren, Z. Ma, P.G. Bruce, Chem. Soc. Rev. **41**, 4909–4927 (2012)
14. I. Abidat, C. Morais, C. Comminges, C. Canaff, J. Rousseau, N. Guignard, T.W. Napporn, A. Habrioux, K.B. Kokoh, J. Mater, Chem. A. **5**, 7173–7183 (**2017**)
15. Y. Wang, X. Cui, Y. Li, L. Chen, Z. Shu, H. Chen, J. Shi, Dalton Trans. **42**, 9448–9452 (2013)
16. M.M. Nair, F. Kleitz, S. Kaliaguine, Chem Cat Chem. **4**, 387–394 (2012)
17. Q. Lu, C.J. Chen, W. Luc, J.G. Chen, A. Bhan, F. Jiao, ACS Catal. **6**, 3506–3514 (2016)
18. S. Fu, C. Zhu, J. Song, M.H. Engelhard, X. Li, D. Du, Y. Lin, ACS Energy Lett. **1**, 792–796 (2016)
19. T. Sun, N. Shan, L. Xu, J. Wang, J. Chen, A.A. Zakhidov, R.H. Baughman, Chem. Mater.**30**, 2018 (1617-1624)
20. E. Loni, M.H. Siadati, A., Shokuhfar, Mater. Today Energy **16**, 100398 (2020).
21. A. Saad, H. Shen, Z. Cheng, R. Arbi, B. Guo, L.S. Hui, K. Liang, S. Liu, J.P. Attfield, A. Turak, J. Wang, M. Yang, Nano-Micro Letters **12**, 1–13 (2020)
22. H.Y. Kim, J.M. Kim, Y. Ha, J. Woo, A. Byun, T.J. Shin, K.H. Park, H.Y. Jeong, H. Kim, J.Y. Kim, S.H. Joo, ACS Catal. **9**, 11242–11254 (2019)

23. R. Ryoo, S.H. Joo, S. Jun, J. Phys, Chem. B. **103**, 7743–7746 (1999)
24. Y. Doi, A. Takai, Y. Sakamoto, O. Terasaki, Y. Yamauchi, K. Kuroda, Chem. Comm. **46**, 6365–6367 (2010)
25. H. Wang, H.Y. Jeong, M. Imura, L. Wang, L. Radhakrishnan, N. Fujita, T. Castle, O. Terasaki, Y. Yamauchi, J. Am, Chem. Soc. **133**, 14526–14529 (2011)
26. J. Fang, L. Zhang, J. Li, L. Lu, C. Ma, S. Cheng, Z. Li, Q. Xiong, H. You, Nat. Commun. **9**, 521 (2018)
27. S.W. Lee, C. Baik, C. Pak, Catal.Today., (2019) https://doi.org/10.1016/j.cattod.2019.12.003
28. S.W. Lee, C. Baik, T.Y. Kim, C. Pak, Catal. Today. (2019). https://doi.org/10.1016/j.cattod.2019.10.004
29. J.K. Shon, H.S. Lee, G.O. Park, J. Yoon, E. Park, G.S. Park, S.S. Kong, M. Jin, J.M. Choi, H. Chang, S. Doo, Nat. Commun. **7**, 11049 (2016)
30. G.S. Armatas, A.P. Katsoulidis, D.E. Petrakis, P.J. Pomonis, M.G. Kanatzidis, Chem. Mater. **22**, 5739–5746 (2010)
31. C.Y. Ma, Z. Mu, J.J. Li, Y.G. Jin, J. Cheng, G.Q. Lu, Z.P. Hao, S.Z. Qiao, J. Am, Chem. Soc. **132**, 2608–2613 (2010)
32. X. Deng, K. Chen, H. Tüysüz, Chem., Mater. **29**, 40–52 (2016)
33. G.H. Moon, M. Yu, C.K. Chan, H. Tüysüz, Angew. Chem. Int. Ed. **131**, 3529–3533 (2019)
34. M. Sakeye, S. Ziller, H. Amenitsch, M. Lindén, J.H. Smått, J. Phys, Chem. C. **120**, 1854–1862 (2016)
35. A. Fischer, J.O. Müller, M. Antonietti, A. Thomas, ACS nano **2**, 2489-2496 (2008).
36. P. Ji, J. Zhang, F. Chen, M. Anpo, J. Phys, Chem. C. **112**, 17809–17813 (2008)
37. D.S. Baek, G.Y. Jung, B. Seo, J.C. Kim, H.W. Lee, T.J. Shin, H.Y. Jeong, S.K. Kwak, S.H. Joo, Adv. Funct. Mater., 1901217 (2019)
38. M.M. Nair, S. Kaliaguine, F. Kleitz, ACS Catal. **4**, 3837–3846 (2014)
39. C. Nguyen-Huy, H. Lee, J. Lee, J.H. Kwak, K An, Appl. Catal. A **5**(118) (2019)
40. H. Tüysüz, Y. Liu, C. Weidenthaler, F. Schüth, J. Am, Chem. Soc. **130**, 14108–14110 (2008)
41. F. Jiao, K.M. Shaju, P.G. Bruce, Angew. Chem. Int. Ed. **44**, 6550–6553 (2005)
42. H. Tüysüz, E.L. Salabaş, E. Bill, H. Bongard, B. Spliethoff, C.W. Lehmann, F. Schüth, Chem. Mater. **24**, 2493–2500 (2012)
43. Y. Shi, Y. Wan, R. Zhang, D. Zhao, Adv. Funct. Mater. **18**, 2436–2443 (2008)
44. F. Jiao, H. Frei, Energy Environ. Sci. **3**, 1018–1027 (2010)
45. W. Lai, L. Zhang, W. Hua, S. Indris, Z. Yan, Z. Hu, B. Zhang, Y. Liu, L. Wang, M. Liu, Y. Wang, Angew. Chem **58**, 11868–11873 (2019)
46. T. Priamushko, R. Guillet-Nicolas, F. Kleitz, Inorganics **7**, 98 (2019)
47. D. Gu, C.J. Jia, C. Weidenthaler, H.J. Bongard, B. Spliethoff, W. Schmidt, F. Schüth, J. Am, Chem. Soc. **137**, 11407–11418 (2015)
48. H. Tüysüz, Y.J. Hwang, S.B. Khan, A.M. Asiri, P. Yang, Nano Res **6**, 47–54 (2013)
49. X. Deng, W.N. Schmidt, H. Tüysüz, Chem. Mater. **26**, 6127–6134 (2014)
50. T. Grewe, X. Deng, C. Weidenthaler, F. Schüth, H. Tüysüz, Chem. Mater **25**, 4926–4935 (2013)
51. Y. Huang, W. Yang, Y. Yu, S. Hao, J. Electroanal, Chem. **840**, 409–414 (2019)
52. Y. Yang, W. Zhou, R. Liu, M. Li, T.E. Rufford, Z. Zhu, ChemElectroChem **2**, 200–203 (2015)
53. X. Deng, C.K. Chan, H. Tüysüz, ACS Appl. Mater. Interfaces **8**(32488-32495) (2016)
54. C. Xiao, X. Lu, C. Zhao, Chem. Comm. **50**, 10122–10125 (2014)
55. Y.J. Sa, K. Kwon, J.Y. Cheon, F. Kleitz, S.H. Joo, J. Mater, Chem. A **1**, 9992–10001 (2013)
56. T. Grewe, X. Deng, H. Tüysüz, Chem. Mater. **26**, 3162–3168 (2014)
57. X. Lu, Y.H. Ng, C. Zhao, ChemSusChem. **7**, 82–86 (2014)
58. W. Wang, S. Xi, Y. Shao, X. Gao, J. Lin, C. Meng, W. Wang, X. Guo, G. Li, ChemElectroChem. **6**, 1846–1852 (2019)
59. Q. Qu, J.H. Zhang, J. Wang, Q.Y. Li, C.W. Xu, X. Lu, Sci. Rep. **7**, 41542 (2017)
60. X. Gao, J. Liu, Y. Sun, X. Wang, Z. Geng, F. Shi, X. Wang, W. Zhang, S. Feng, Y. Wang, K. Huang, Inorg Chem Front. **6**, 3295–3301 (2019)
61. I. Abidat, N. Bouchenafa-Saib, A. Habrioux, C. Comminges, C. Canaff, J. Rousseau, T.W. Napporn, D. Dambournet, O. Borkiewicz, K.B. Kokoh, J. Mater, Chem. A **3**, 17433–17444 (2015)
62. X. Deng, S. Öztürk, C. Weidenthaler, H. Tüysüz, ACS Appl. Mater. Interfaces. **9**, 21225–21233 (2017)
63. C. Broicher, F. Zeng, J. Artz, H. Hartmann, A. Besmehn, S. Palkovits, R. Palkovits, ChemCatChem. **11**, 412–416 (2019)
64. N.T. Suen, S.F. Hung, Q. Quan, N. Zhang, Y.J. Xu, H.M. Chen, Chem. Soc. Rev **46**, 337–29365 (2017)
65. Q. Qu, G.L. Pan, Y.T. Lin, C.W. Xu, Int. J. Hydrog. Energy **43**, 14252–14264 (2018)
66. C. Mahala, M.D. Sharma, M. Basu, Electrochim. Acta **273**, 462–473 (2018)
67. W. Xu, Z. Wu, S. Tao, J. Mater. Chem. A **4**, 16272–16287 (2016)
68. J. Behnken, M. Yu, X. Deng, H. Tüysüz, C. Harms, A. Dyck, G. Wittstock, ChemElectroChem **6**, 3460–3467 (2019)
69. W. Li, J. Liu, D. Zhao, Nat. Rev. Mater. **1**, 1–17 (2016)
70. S. Sun, X. Zhao, M. Yang, L. Wu, Z. Wen, X. Shen, Sci. Rep. **6**, 19564 (2016)
71. S. Sun, Z. Wen, J. Jin, Y. Cui, Y. Lu, Micropor. Mesopor. Mat **169**, 242–247 (2013)
72. R. Zhao, Q. Li, C. Wang, L. Yin, Electrochim. Acta. **197**, 58–67 (2016)
73. G.O. Park, J. Yoon, J.K. Shon, Y.S. Choi, J.G. Won, S.B. Park, K.H. Kim, H. Kim, W.S. Yoon, J.M. Kim, Adv. Funct. Mater. **26**, 2800–2808 (2016)
74. Z. Lin, W. Yue, D. Huang, J. Hu, X. Zhang, Z.Y. Yuan, X. Yang, RSC Adv **2**, 1794–1797 (2012)
75. G. Wu, Q. Ren, W. Xing, J. Han, P. Li, J. Cheng, S. Wu, R. Zou, J. Hu, Front Chem **7**, 521 (2019)
76. P.M. Ette, K. Selvakumar, S.M.S. Kumar, K. Ramesha, Electrochim. Acta **310**(184-194) (2019)
77. J. Yang, T. Zhou, R. Zhu, X. Chen, Z. Guo, J. Fan, H.K. Liu, W.-X. Zhang, Adv. Mater. Interfaces **3**, 1500464 (2016)
78. C. Teng, F. Yang, M. Sun, K. Yin, Q. Huang, G. Fu, C. Zhang, X. Lu, J. Jiang, Chem. Sci **10**, 7600–7609 (2019)
79. P. Li, W. Sun, Q. Yu, P. Yang, J. Qiao, Z. Wang, D. Rooney, K. Sun, Solid State Ion **289**, 17–22 (2016)
80. Y. Li, L. Zou, J. Li, K. Guo, X. Dong, X. Li, X. Xue, H. Zhang, H. Yang, Electrochim. Acta **129**, 14–20 (2014)
81. Y. Ren, Z. Ma, P.G. Bruce, J. Mater, Chem. **22**, 15121–15127 (2012)
82. P. Li, W. Sun, Q. Yu, M. Guan, J. Qiao, Z. Wang, D. Rooney, K. Sun, Mater. Lett **158**, 84–87 (2015)
83. F. Cheng, Z. Tao, J. Liang, J. Chen, Chem. Mater**20**, 667-681 (2007).
84. P.G. Bruce, B. Scrosati, J.M. Tarascon, Angew. Chem **47**, 2930–2946 (2008)
85. L. Ji, Z. Lin, M. Alcourlabi, X. Zhang, Energy Environ. Sci **4**(2682-2699) (2011)
86. G.O. Park, J. Yoon, E. Park, S.B. Park, H. Kim, K.H. Kim, X. Jin, T.J. Shin, H. Kim, W.S. Yoon, J.M. Kim, ACS nano. **9**, 5470–5477 (2015)
87. Y. Ren, A.R. Armstrong, F. Jiao, P.G. Bruce, J. Am, Chem. Soc **132**, 996–1004 (2009)

88. M.J. Armstrong, C. O'Dwyer, W.J. Macklin, J.D. Holmes, Nano Res **7**, 1–62 (2014)
89. P. Sengodu, C. Bongu, M. Perumal, M. Paramasivam, J. Alloys Comp. **714**, 603–609 (2017)
90. H. Sun, X. Sun, T. Hu, M. Yu, F. Lu, J. Lian, J. Phys. Chem. C. **118**, 2263–2272 (2014)
91. K.M. Shaju, F. Jiao, A. Débart, P.G. Bruce, Phys. Chem. Chem. Phys **9**, 1837 (2007)
92. Y. Li, Y.S. Hu, M.M. Titirici, L. Chen, X. Huang, Adv. Energy Mater. **6**, 1600659 (2016)
93. R. Alcántara, M. Jaraba, P. Lavela, J.L. Tirado, Chem. Mater **14**, 2847–2848 (2002)
94. K.P. Yao, M. Risch, S.Y. Sayed, Y.L. Lee, J.R. Harding, A. Grimaud, N. Pour, Z. Xu, J. Zhou, A. Mansour, F. Bardé, Energy Environ. Sci **8**, 2417–2426 (2015)
95. L. Ma, S. Chen, H. Li, Z. Ruan, Z. Tang, Z. Liu, Z. Wang, Y. Huang, Z. Pei, J.A. Zapien, C. Zhi, Energy Environ. Sci **11**, 2521–2530 (2018)
96. C. Xiao, X. Zhang, T. Mendes, G.P. Knowles, A. Chaffee, D.R. MacFarlane, J. Phys, Chem. C **120**, 23976–23983 (2016)
97. W.J. Zhou, J. Zhang, T. Xue, D.D. Zhao, H.L. Li, J. Mater, Chem. **18**, 905–910 (2008)
98. Y. Wang, J. Guo, T. Wang, J. Shao, D. Wang, Y.W. Yang, *Nanomaterials* **5**, 1667–1689 (2015)
99. M.B. Zheng, J. Cao, S.T. Liao, J.S. Liu, H.Q. Chen, Y. Zhao, W.J. Dai, G.B. Ji, J.M. Cao, J. Tao, J. Phys, Chem. C **113**, 3887–3894 (2009)
100. L. An, Q. Ren, W. Li, K. Xu, Y. Cao, T. Ji, R. Zou, Z. Chen, J. Hu, J. Mater, Chem. A **3**, 11503–11510 (2015)
101. A. Pendashteh, S.E. Moosavifard, M.S. Rahmanifar, Y. Wang, M.F. El-Kady, R.B. Kaner, M.F. Mousavi, Chem. Mater. **27**, 3919–3926 (2015)
102. W.H. Hung, S.N. Lai, C.Y. Su, M. Yin, D. Li, X. Xue, C.M. Tseng, Appl. Phys. Lett **107**, 073904 (2015)
103. J. Rosen, G.S. Hutchings, F. Jiao, J. Am, Chem. Soc **135**, 4516–4521 (2013)
104. J. Rosen, G.S. Hutchings, F. Jiao, J. Catal **310**, 2–9 (2014)
105. X. Deng, H.J. Bongard, C.K. Chan, H. Tüysüz, ChemSusChem **9**, 409–415 (2016)
106. C.I. Ahn, Y.M. Park, J.M. Cho, D.H. Lee, C.H. Chung, B.G. Cho, J.W. Bae, CatalSurvAsia. **20**, 210–230 (2016)
107. J.M. Cho, S.R. Lee, J. Sun, N. Tsubaki, E.J. Jang, J.W. Bae, ACS Catal. **7**, 5955–5964 (2017)
108. C.I. Ahn, H.M. Koo, J.M. Jo, H.S. Roh, J.B. Lee, Y.J. Lee, E.J. Jang, J.W. Bae, Appl Catal B. **180**, 139 (2016)
109. Y.M. Park, D.H. Lee, Y.J. Lee, H.S. Roh, C.H. Chung, J. Wook Bae, ChemCatChem **11**, 1707–1721 (2019)
110. A. Sápi, G. Halasi, A. Grósz, J. Kiss, A. Kéri, G. Ballai, G. Galbács, Á. Kukovecz, Z., Kónya. J. Nanosci. Nanotechnol **19**, 436–441 (2019)
111. S. Cui, L. Li, Y. Ding, J. Zhang, Q. Wu, Z. Hu, Nano Res. **10**, 2482–2494 (2017)
112. H. Arandiyan, Y. Wang, H. Sun, M. Rezaei, H. Dai, Chem Comm **54**, 6484–6502 (2018)
113. J. Suntivich, K.J. May, H.A. Gasteiger, J.B. Goodenough, Y. Shao-Horn, Science **334**, 1383–1385 (2011)
114. Y. Wang, X. Cui, Y. Li, Z. Shu, H. Chen, J. Shi, Micropor. Mesopor. Mat **176**, 8–15 (2013)
115. R.K.C. de Lima, M.S. Batista, M. Wallau, E.A. Sanches, Y.P. Mascarenhas, E.A. Urquieta-González, Appl. Catal. B **90**, 441–450 (2009)
116. Y. Wang, J. Ren, Y. Wang, F. Zhang, X. Liu, Y. Guo, G. Lu, J. Phys. Chem. **C112**, 15293–15298 (2008)
117. J.H. Yang, H.J. Sun, G. Park, J.C. An, J. Shim, J. Electroceram **41**, 80–87 (2018)
118. H. Du, R.-M. Kong, X. Guo, F. Qu, J. Li, Nanoscale **10**, 21617–21624 (2018)
119. P. Mei, J. Kim, N.A. Kumar, M. Pramanik, N. Kobayashi, Y. Sugahara, Y. Yamauchi, Joule. **2**, 2289–2306 (2018)
120. P. Mei, Y. Yamauchi, M. Pramanik, A. Fatehmulla, A.M. Aldhafiri, W.A. Farooq, Y. Bando, M. Shiddiky, Y.V. Kaneti, J. Lin, Y. Kim, Electrochem. Commun **104**, 106476 (2019)
121. P. He, X.Y. Yu, X.W. Lou, Angew. Chem. Int. Ed.**56**, 3897–3900 (2017)
122. M. Pramanik, S. Tominaka, Z.L. Wang, T. Takei, Y. Yamauchi, Angew. Chem **129**, 13693–13697 (2017)
123. J. Wang, Z. Liu, Y. Zheng, L. Cui, W. Yang, J. Liu, J. Mater, Chem. A **5**, 22913–22932 (2017)
124. 108. Y. Huang, M. Li, W. Yang, Y. Yu, S. Hao, 3D ordered mesoporous cobalt ferrite phosphides for overall water splitting, Sci. China Mater **63** , 240–248(2019).
125. X. Gao, D. Zhou, Y. Chen, W. Wu, D. Su, B. Li, G. Wang, Commun. Chem **2**, 1–10 (2019)
126. G. Jiang, H. Han, W. Zhuang, X. Xu, S. Kaskel, F. Xu, H. Wang, J. Mater, Chem. A **7**, 17561–17569 (2019)
127. A. Saad, Z. Cheng, X. Zhang, S. Liu, H. Shen, T. Thomas, J. Wang, M. Yang, Adv. Mater. Interfaces **6**, 1900960 (2019)
128. S. Meyer, H. Beyer, K. Köhler, A.H. Jensen, E. Christensen, N.J. Bjerrum, Micropor. Mesopor. Mat **211**, 147–151 (2015)
129. G. Jiang, Y. Qiu, Q. Lu, W. Zhuang, X. Xu, S. Kaskel, F. Xu, H. Wang, ACS Appl. Mater. Interfaces **11**, 41188–41195 (2019)
130. Y. Shi, Y. Wan, R. Liu, B. Tu, D. Zhao, J. Am, Chem. Soc **129**, 9522–9531 (2007)
131. L. Jin, B. Liu, Y. Wu, S. Thanneeru, J. He, ACS Appl. Mater. Interfaces **9**, 36837 (2017)
132. B.T. Yonemoto, G.S. Hutchings, F. Jiao, J. Am, Chem. Soc **136**, 8895–8898 (2014)
133. A. Saad, H. Shen, Z. Cheng, Q. Ju, H. Guo, M. Munir, A. Turak, J. Wang, M. Yang, ACS Appl. Energy Mater. (2020). https://doi.org/10.1021/acsaem.9b02155